Ore Geology Reviews 154 (2023) 105314

Contents lists available at ScienceDirect

Ore Geology Reviews

journal homepage: www.elsevier.com/locate/oregeorev

The Paleoproterozoic Zhaigou banded iron formation in the Fuping Complex, North China Craton: Geochemistry, geochronology and implications for genesis and tectonic setting

Tao Zeng [a], Li Tang [a,b,*], Han-Hui Wang [a], M. Santosh [a,c], Yuan-Ming Sheng [a,b]

[a] School of Earth Sciences and Resources, China University of Geosciences Beijing, 29 Xueyuan Road, Beijing 100083, China
[b] Key Laboratory of Tectonic Controlled Mineralization and Oil Reservoir of Ministry of Natural Resources, Chengdu University of Technology, China
[c] Department of Earth Science, University of Adelaide, Adelaide SA 5005, Australia

ARTICLE INFO

Keywords:
Banded iron formation
Algoma-type
Zhaigou BIF deposit
Paleoproterozoic
North China Craton

ABSTRACT

Precambrian Banded iron formations (BIFs) provide important insights on the chemical composition of ancient seawater, as well as the tectonic setting of their formation. The Precambrian BIFs deposits in the North China Craton are widely distributed in the Archean greenstone belts and are composed predominantly of Neoarchean Algoma-type including those in the Anshan-Benxi and eastern Hebei areas of the Eastern Block, together with minor Paleoproterozoic Superior-type BIFs in the southern segment of the trans-North China Orogen. The Zhaigou BIF deposit is associated with Paleoproterozoic Wanzi supracrustal sequence and amphibolite in the Fuping Complex in central North China Craton. Here, we present petrological, geochronological and geochemical data of the *meta*-sedimentary rocks, BIF ores and amphibolites from the Zhaigou BIF deposit in the Fuping Complex for the first time to constrain the formation age, source characteristics and depositional setting, and evaluate the redox states of the Paleoproterozoic seawater. Whole-rock geochemical data show that the BIF ores are enriched in HREE with low $(La/Yb)_{PAAS}$ values (0.037–0.073), and exhibit positive Eu (3.34–6.21) and Pr (1.05–1.10) anomalies. The PAAS-normalized REY patterns resemble 1:100 mixture of high-temperature hydrothermal fluid and seawater, indicating the involvement of the two end members. In combination with whole-rock geochemical data of BIF ores, trace elements of magnetite and U-Pb ages of detrital zircons from the *meta*-sedimentary rocks, we propose that crustal components from the Fuping TTG gneiss also contributed to the BIFs. The geochemical features suggest that the protolith of amphibolite is basalt formed in island arc setting. The negative Ce anomaly ($Ce/Ce^* = 0.81 \sim 0.90$) indicates the deposition of the Zhaigou BIF ore in an oxidizing environment. Zircon U-Pb data on the BIF ore yield weighted mean $^{207}Pb/^{206}Pb$ ages of 2028 ± 33 Ma and 1874 ± 52 Ma, representing the formation age of the Zhaigou BIF deposit and the subsequent metamorphic event, respectively. The Zhaigou BIF deposit belongs to the Algoma-type which shows close association with the Paleoproterozoic sedimentary sequence and basaltic magmatism in oceanic island arc setting. The Paleoproterozoic seawater forming the Zhaigou deposit was oxidized after the Great Oxygenation Event (GOE) during the terrane assembly in the trans-North China Orogen.

1. Introduction

Banded iron formations (BIFs) are marine sedimentary rocks containing at least 15 % iron and characterized by Fe- and Si-rich interlayers and are dominantly of Archean and Paleoproterozoic age (James, 1954; Jiang et al., 2022; Santosh and Groves, 2022). Based on depositional environments and rock associations, two types of BIF deposits are broadly defined: the Superior-type and Algoma-type (Bekker et al., 2010; Konhauser et al., 2017). The Superior-type BIF deposits are associated with quartzites, carbonates, and shales, and formed in relatively stable sedimentary basins (Gross, 1980; Li et al., 2022). By contrast, the Algoma-type BIFs are associated with volcanic or volcaniclastic rocks, greywackes and shales. Most Algoma-type BIFs formed in arc/back-arc basins and were preserved in Archean greenstone belts (Bekker et al., 2010; Dodd et al., 2022). The deposition of the two BIF types in oceanic basins can reflect the secular changes of atmosphere,

* Corresponding author.
E-mail address: ltang@cugb.edu.cn (L. Tang).

https://doi.org/10.1016/j.oregeorev.2023.105314
Received 24 September 2022; Received in revised form 12 December 2022; Accepted 19 January 2023
Available online 23 January 2023

hydrosphere (e.g. chemical composition and redox states of paleo-oceans) and lithosphere (Derry and Jacobsen, 1990; Bau and Dulski, 1996; Bolhar et al., 2004; Konhauser et al., 2017; Sindhuja et al., 2020; Dodd et al., 2022).

In China, BIFs are the principal source for iron and most of the BIFs are distributed in the North China Craton (NCC). The BIF deposits in the NCC are mainly Algoma-type and show mineralization age of Neoarchean (2.7 ~ 2.5 Ga), such as the typical BIF deposits in the Anshan-Benxi, Jidong, Luxi, Wutai, Wuyang, Guyang and other regions (Zhai and Santosh, 2011, 2013; Wang et al., 2020b; Sun et al., 2020; Tong et al., 2019). Paleoproterozoic (2.4 ~ 2.2 Ga) Superior-type BIF deposits are rarely distributed in the NCC, with a few examples distributed in Yuanjiacun, Shanxi, Huoqiu and Anhui (Lan et al., 2014a, 2014b; Yang et al., 2014; Wang et al., 2015). The Fuping Complex in the central segment of the trans-North China Orogen (TNCO) preserves metamorphosed mafic–ultramafic rocks, TTG gneisses, *meta*-sedimentary rocks and minor BIFs. Previous studies mainly focused on the geochronology, geochemistry and isotopes of TTG gneisses and *meta*-mafic rocks of the Fuping Complex (Cheng et al., 2004; Zhao et al., 2007; Tang et al., 2015, 2016; Wang et al., 2020a). Tang et al. (2015) reported three types of amphibolites associated with marble, leptite and BIF, and proposed that these *meta*-basaltic rocks were formed in arc setting during 2.1–2.0 Ga. The Zhaigou BIF deposit is closely associated with the Paleoproterozoic Wanzi supracrustal sequence and amphibolite in the Fuping Complex. Therefore, the Zhaigou BIF represents an ideal case to evaluate the origin of Paleoproterozoic BIF deposit and the associated depositional setting and redox condition of ancient seawater.

In this study, we present results from systematic field investigation, petrology and mineralogy, zircon U–Pb geochronology and whole-rock geochemistry of BIF ore, biotite gneiss and amphibolite to constrain the formation age, source characteristics and depositional setting of the Zhaigou BIF deposit, as well as to evaluate the redox states of the Paleoproterozoic seawater.

2. Regional geology

2.1. Geological setting of the NCC

The North China Craton (NCC) records a prolonged and intricate tectonic evolution history from ~ 3.8 Ga, and the crustal growth, tectonic framework and metallogenesis have attracted wide attention in the past decades (e.g., Zhai and Santosh, 2011, 2013; Trap et al., 2012; Zhao and Zhai, 2013; Tang and Santosh, 2018a, 2018b; Groves and Santosh, 2021; Xu et al., 2022; Liou et al., 2022; Liu et al., 2022). The NCC consists of Archean to Paleoproterozoic metamorphic basement and Mesoproterozoic to Cenozoic unmetamorphosed cover sequences (Zhai and Santosh, 2011; Zhao and Zhai, 2013; Guo et al., 2022; Liou et al., 2022). Diverse models were proposed for the tectonic division of the Precambrian basement of the NCC (e.g., Zhao et al., 2005; Tang and Santosh, 2018a) among which the more popular model divides the NCC

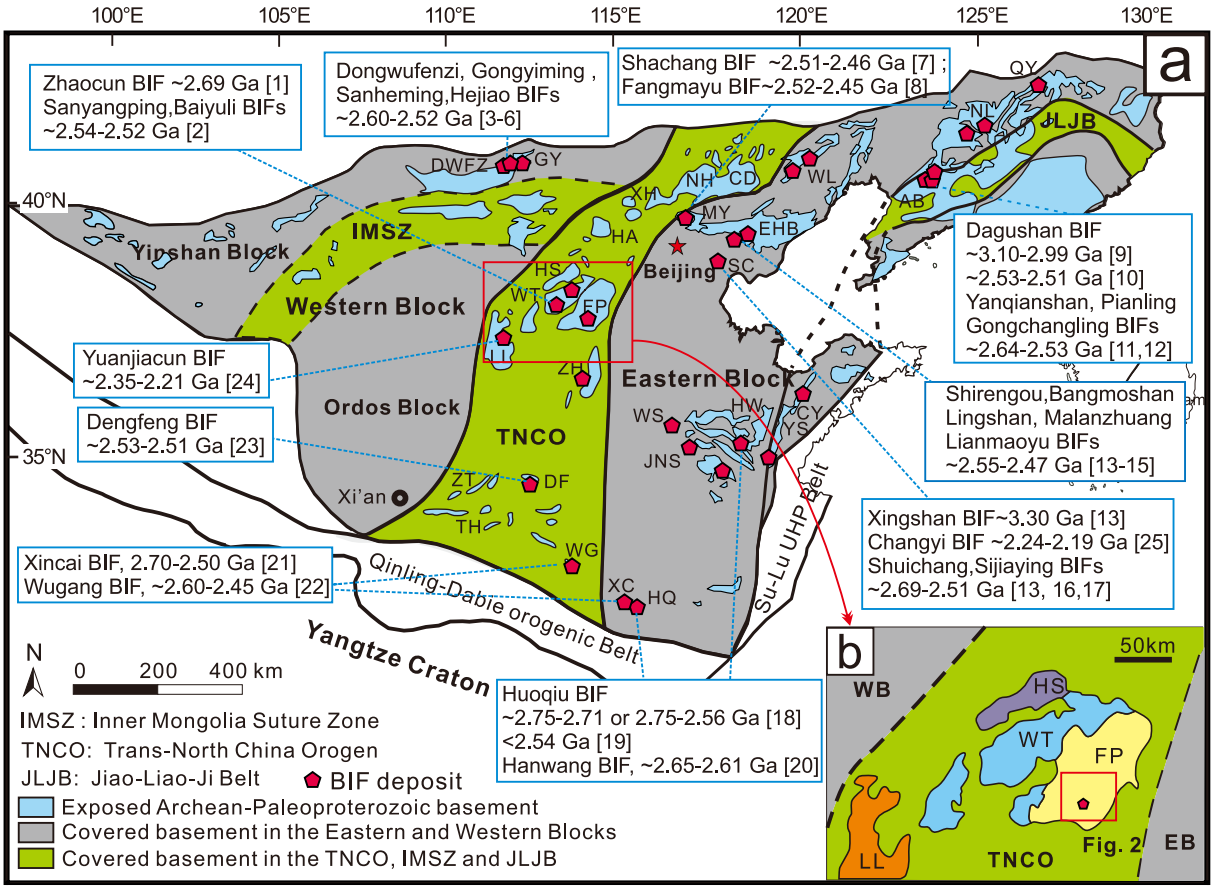

Fig. 1. (a) Tectonic subdivision of the North China Craton, showing the basement rocks in the Eastern Block, Western Block and trans-North China Orogen (modified after Zhao et al., 2005). Abbreviations of metamorphic complexes: CD, Chengde; NH, Northern Heibei; XH, Xuanhua; HA, Huai'an; HS, Hengshan; WT, Wutai; FP, Fuping; LL, Lüliang; ZH, Zanhuang; ZT, Zhongtiao; DF, Dengfeng; TH, Taihua; WB, Western Block; EB, Eastern Block. [1] Wang et al. (2014); [2] Han et al. (2017); [3] Liu et al. (2014); [4] Ma et al. (2014); [5] Liu et al. (2012); [6] Wang et al. (2020b); [7] Shi and Shi. (2016); [8] Shi and Shi. (2017); [9] Dai et al. (2014); [10] Tong et al. (2019); [11] Li et al. (2016); [12] Sun et al. (2020); [13] Han et al. (2014); [14] Li et al. (2015); [15] Zhang et al. (2012b); [16] Cui et al. (2014); [17] Zhang et al. (2011); [18] Liu and Yang. (2015); [19] Hou et al. (2017); [20] Shi et al. (2019); [21] Lan et al. (2019a); [22] Liu et al. (2018); [23] Huang et al. (2019); [24] Wang et al. (2015); [25] Lan et al. (2014a).

into three major tectonic units, including the Western Block (WB), Eastern Block (EB) and the intervening trans-North China Orogen (TNCO) (Fig. 1; Zhao et al., 2005; Zhao and Zhai, 2013). Two Paleoproterozoic orogenic belts were identified from the Eastern Block and the Western Block, namely the Jiao-Liao-Ji Belt and the Khondalite Belt, which are composed predominantly of Paleoproterozoic metamorphosed volcano-sedimentary rocks and TTG gneisses. The north–south trending TNCO incorporates several basement terranes which include Taihua, Dengfeng, Zhongtiao, Zanhuang, Lüliang, Fuping, Wutai, Hengshan, Huai'an, Xuanhua, Northern Hebei and Chengde Complexes from the south to north (Fig. 1a). The basement rocks comprise Neoarchean to Paleoproterozoic TTG gneisses, *meta*-supracrustal rocks, syn- to post-tectonic granitoids, mafic dykes, and ultramafic to mafic rocks (Wei et al., 2014; Zhai et al., 2021). The linear structural belts (Trap et al., 2007; Zhang et al., 2012a), retrograde eclogites and high pressure granulites (Guo et al., 2002), clockwise P–T paths involving near isothermal decompression and metamorphic ages of 1.96–1.80 Ga (Tang et al., 2017, 2023; Zhao et al., 2012) define the TNCO as a collisional orogenic belt between the EB and WB.

An alternate model considers that the NCC is composed of a number of small Archean nuclei surrounded by greenstone belts and that the closure of the intervening oceans welded them together (Zhai and Santosh, 2011; Zhao and Zhai, 2013; Tang and Santosh, 2018b). Bai et al. (1996) proposed that the NCC was amalgamated by microblocks along several Neoarchean greenstone belts. Wu et al. (1998) suggested that the NCC comprises five microblocks (Jiaoliao, Qianhuai, Jinji, Yuwan and Mongshan) assembled at ~ 2.5 Ga, whereas Zhang et al. (1998) proposed that up to fifteen contrasting microblocks/terranes can be identified in the NCC. Zhai et al. (2000) divided the NCC into six microblocks including the Alashan, Jining, Fuping, Jiaoliao, Xuchang and Qianhuai blocks and these microblocks were amalgamated together at the late Neoarchean. Recent studies proposed seven microblocks as the fundamental parts of the Archean NCC, including the Jiaoliao Block (JL), Qianhuai Block (QH), Ordos Block (OR), Jining Block (JN), Xuchang Block (XCH), Xuhuai Block (XH) and Alashan Block (ALS) (Zhai and Santosh, 2011; Santosh et al., 2016; Tang and Santosh, 2018b).

2.2. Brief summary of BIFs in the NCC

Most of the Precambrian BIF deposits in the Archean-Paleoproterozoic greenstone belts of the NCC belong to Algoma-type, with a few Superior-type BIFs found in the southern segment of the TNCO (Fig. 1a; Zhang et al., 2012a; Zhai and Santosh, 2011, 2013; Dai et al., 2016; Liu et al., 2014; Huang et al., 2019). In the WB, BIF deposits are mainly distributed in the Guyang greenstone belt with a formation age of 2.60–2.52 Ga (Liu et al., 2012, 2014; Ma et al., 2014; Wang et al., 2020b). Liu et al. (2014) and Wang et al. (2020) proposed that the Guyang greenstone belt was formed in a geodynamic setting of mantle plume erupting within a subduction zone, and that the BIFs were deposited in arc-related basins. The BIF deposits in the TNCO are mostly distributed in the central and southern segments, including the Wutai greenstone belt (Wang et al., 2014; Han et al., 2017), the Dengfeng greenstone belt (Huang et al., 2019) and the Taihua complex (Liu et al., 2018). These BIFs were formed in late Neoarchean with a peak mineralization age of ~ 2.54 Ga (Fig. 1a) and underwent greenschist- to granulite-facies metamorphism during 2.51–2.50 Ga (Wang et al., 2014). The BIFs in the EB spread along the Anshan-Benxi-Qingyuan belt (Dai et al., 2014; Tong et al., 2019; Li et al., 2016; Sun et al., 2020), Eastern Hebei (Zhang et al., 2011; Zhang et al., 2012b; Han et al., 2014; Cui et al., 2014; Li et al., 2015), Western Shandong (Shi et al., 2019), Southern Xincai (Lan et al., 2019a,b) and Huoqiu (Liu and Yang, 2015; Hou et al., 2017). The depositional ages of these BIFs were approximately constrained to be 2.70–2.47 Ga (Fig. 1a). Tang and Santosh (2018b) proposed that these Neoarchean BIF deposits are mainly distributed along the 2.5 Ga granite-greenstone belts and formed in arc-related oceanic slab or back-arc basin during the microblock amalgamation process. The Paleoproterozoic BIFs in the NCC are rare, including the Changyi BIF (~2.24–2.19 Ga) in the Western Shandong (Lan et al., 2014a) and Yuanjiacun BIF (~2.35–2.21 Ga) in the Lüliang Complex (Wang et al., 2015).

2.3. Geology of the Fuping Complex and sample details

The Fuping Complex (FPC), located at the central part of the TNCO (Fig. 1b), consists of TTG gneisses, Longquanguan augen gneisses, Wanzi supracrustal rocks and Nanying granitic gneisses (Fig. 2; Zhao et al., 2000, 2002). The TTG gneisses have undergone migmatization, amphibolite- to granulite-facies metamorphism and polyphase deformation, and are composed of medium-grained tonalitic, trondhjemitic, granodioritic and dioritic gneisses (Zhao et al., 2007). The Longquanguan augen gneisses include the Maheqing Formation, granodioritic gneisses, monzogranitic gneisses, and mylonitized granitic pegmatites (Cheng et al., 2004). The Longquanguan augen gneisses show fault contact with the Fuping TTG gneisses and the Wanzi supracrustal sequence (Zhao et al., 2002). The Wanzi supracrustal sequence is represented by felsic and pelitic gneisses, pelitic schists, calc-silicates, marbles, and amphibolites (Xia et al., 2006; Ren et al., 2013). It forms a 100 km long and 15 km wide NE–SW trending fold belt in the southern part, and shows overprints of greenschist- to granulite-facies metamorphism (Zhao et al., 2002; Tang et al., 2023). The Nanying gneissic granites are mainly composed of fine- to medium-grained, weakly-foliated and gneissic monzogranite, granodiorite and granite. The Nanying gneissic granites intrude into the Fuping TTG gneisses with consistent foliation, implying that they experienced same deformational event (Zhao et al., 2002). Zircon U–Pb data reveals that the Fuping TTG gneisses and the Longquanguan augen gneisses were emplaced at 2.52–2.48 Ga and ~ 2.54 Ga (Guan et al., 2002; Zhao et al., 2002; Tang et al., 2016). The Wanzi supracrustal assemblage is considered to have been deposited between 2.10 and 1.84 Ga (Xia et al., 2006), 1.95–1.84 Ga (Tang et al., 2015) or 2.5–2.1 Ga (Ren et al., 2013). The Nanying gneissic granites were emplaced at 2.10–2.02 Ga in a subduction related island arc setting (Guan et al., 2002; Tang et al., 2015) or rift setting (Wang et al., 2020a).

The Zhaigou BIF deposit is exposed in the southern part of the FPC (38°28′15″N; 113°53′0.42″E). The BIF ores show close association with amphibolite and biotite gneiss of the Wanzi supracrustal sequence (Figs. 2, 3). In this study, seventeen representative samples were collected from the Zhaigou BIF deposit, including eight biotite gneisses, six amphibolites and three BIF ores (Supplementary Table 1). The amphibolites and biotite gneisses associated with BIFs show moderate to high degrees of deformation (Fig. 3a-c). The individual layers of BIFs are generally several centimeters in thickness and parallel to the bedding or foliation of wall rocks (Fig. 3c-e). The BIFs consist of quartz- andiron-rich interlayers which range from 1 to 10 mm or several centimeters in thickness (Fig. 3e-f and 4d-e). The mineral assemblage of the BIFs comprises quartz, magnetite, hornblende, plagioclase, chlorite, pyrite and hematite (Fig. 4d-i). Some portions are rich in magnetite, showing magnetite + hornblende, magnetite + quartz and magnetite + chlorite layers (Fig. 4d, 4e). Amphibolites are mainly composed of hornblende + plagioclase + quartz + magnetite ± garnet (Fig. 4a-b). Biotite gneisses are gray white in color, medium-grained, and characterized by the mineral assemblage of quartz + plagioclase + biotite + hornblende ± garnet (Fig. 4c).

3. Analytical techniques

3.1. Zircon U-Pb dating

Biotite gneiss samples (21FP-21A, 21FP-26 and 21FP-28) and BIF ore sample 21FP-21B were chosen for zircon U-Pb isotope and trace element analyses. Zircon grains were separated using standard techniques including heavy liquid separation, magnetic separation and handpicking

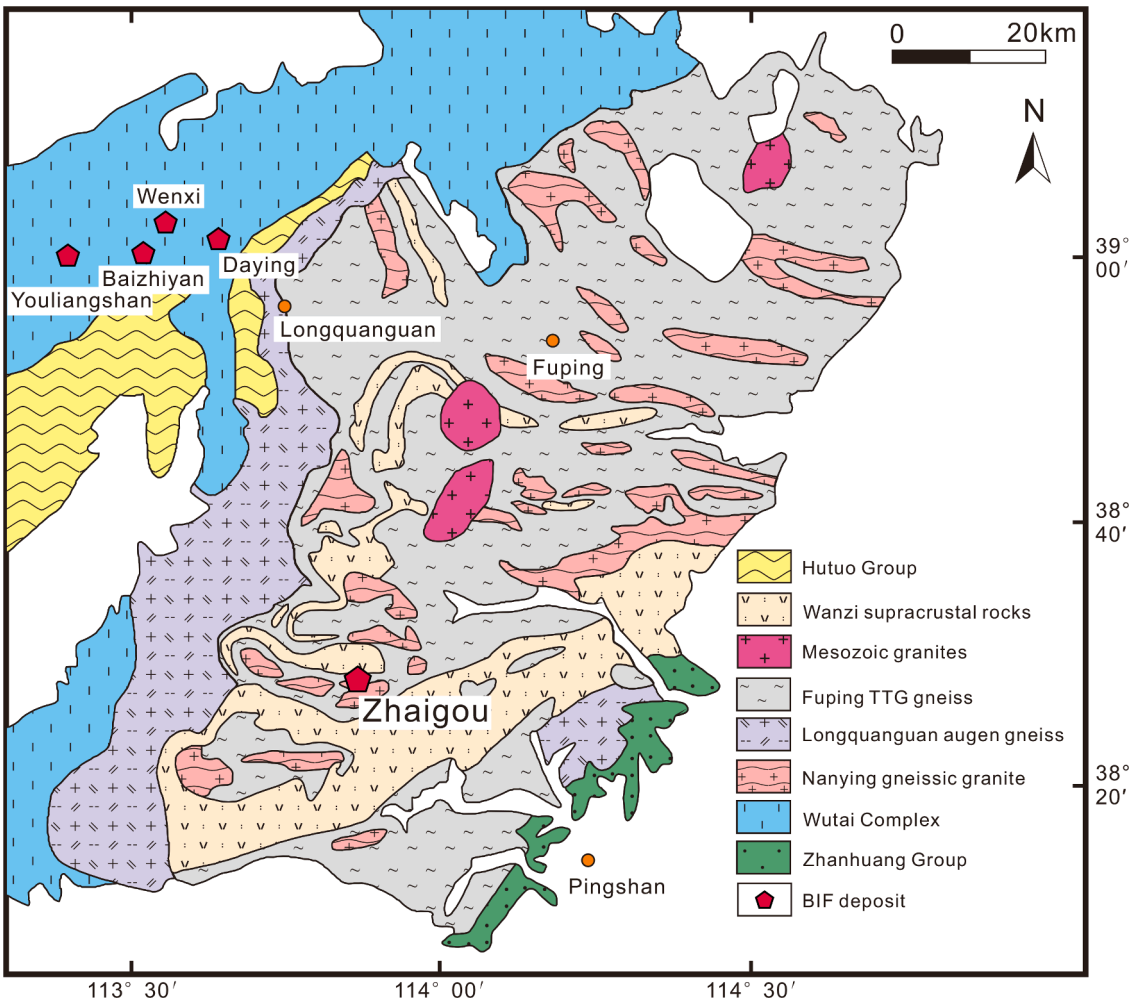

Fig. 2. Geological map of the Fuping Complex within the trans-North China Orogen (modified after Zhao et al., 2000).

under a binocular microscope at the Langfang Honesty Geological Services Co., ltd. China. The polished mount was photographed under cathodoluminescence (CL), transmitted and reflected light. Zircon U-Pb isotopic dating and trace element analyses were completed by LA-ICP-MS at China University of Geosciences, Beijing. The ion signal strength was obtained using Thermo Fisher X Series 2 inductively coupled plasma mass spectrometer (ICPMS). In the laser ablation process, helium was used as carrier gas and argon as compensation gas to adjust the sensitivity. All zircon data were acquired in single spot ablation mode with a spot size of 35 μm. Zircon 91,500 was used as external standard for isotopic fractionation correction. A set of analyses was performed for every 5 sample points, followed by 2 analyses for 91500. The U-Th-Pb isotope ratio shift related to the analytical time was corrected by linear interpolation using the change of 91,500 (Liu et al., 2010). Data reduction was performed using Isoplot (ver. 4.15) (Ludwig, 2012) and ICPMSDataCal (ver. 10.7) (Liu et al., 2010).

3.2. Whole-rock major and trace elements

Whole-rock major and trace elements were measured at the Sample Solution Analytical Technology Co., ltd., Wuhan, China. Sample powders (~50 mg) were dissolved in the mixture of distilled HNO_3-HF in the Teflon bomb at 190 °C for > 24 h. After the complete digestion, the samples were evaporated to dryness on a hotplate at 140 °C. 1 mL distilled HNO_3 was added and evaporated to dryness again, following which 1 mL HNO_3, 1 mL MQ water and 1 mL internal standard solution (1 ppm Indium) were added and hermetically heated to 190 °C for > 12 h. The final solution was transferred to a polyethylene bottle and diluted to 100 g by 2 % HNO_3 for analysis. Two standard materials (basalt BHVO-2 and rhyolite RGM-2) were used to monitor the analytical quality. The analyses were conducted by an Agilent 7700e Inductively Coupled Plasma Mass Spectrometry (ICP-MS). The procedural blanks for each element are lower than 0.1 ppb (mostly lower than 0.01 ppb).

3.3. In situ analysis of magnetite

Major and trace elements of magnetite were analyzed in situ by LA-ICP-MS at the Wuhan Sample Solution Analytical Technology Co., ltd., Wuhan, China. Detailed analytical conditions for the laser ablation system and the ICPMS instrument, and process of data reduction are same with the description in Zong et al. (2017). An Agilent 7700e ICP-MS instrument equipped with a GeolasPro laser ablation system was used to acquire ion-signal intensities. Helium was used as carrier gas and argon was applied as the make-up gas (Hu et al., 2015). The spot size was 32 μm and the laser frequency was 5 Hz. The magnetite trace element compositions were calibrated by the NIST 610 and NIST 612 standards (Liu et al., 2008). Each analysis incorporated a background acquisition of approximately 20–30 s followed by 50 s of data acquisition from the sample. An Excel-based software ICPMSDataCal was used to conduct the results (Liu et al., 2008).

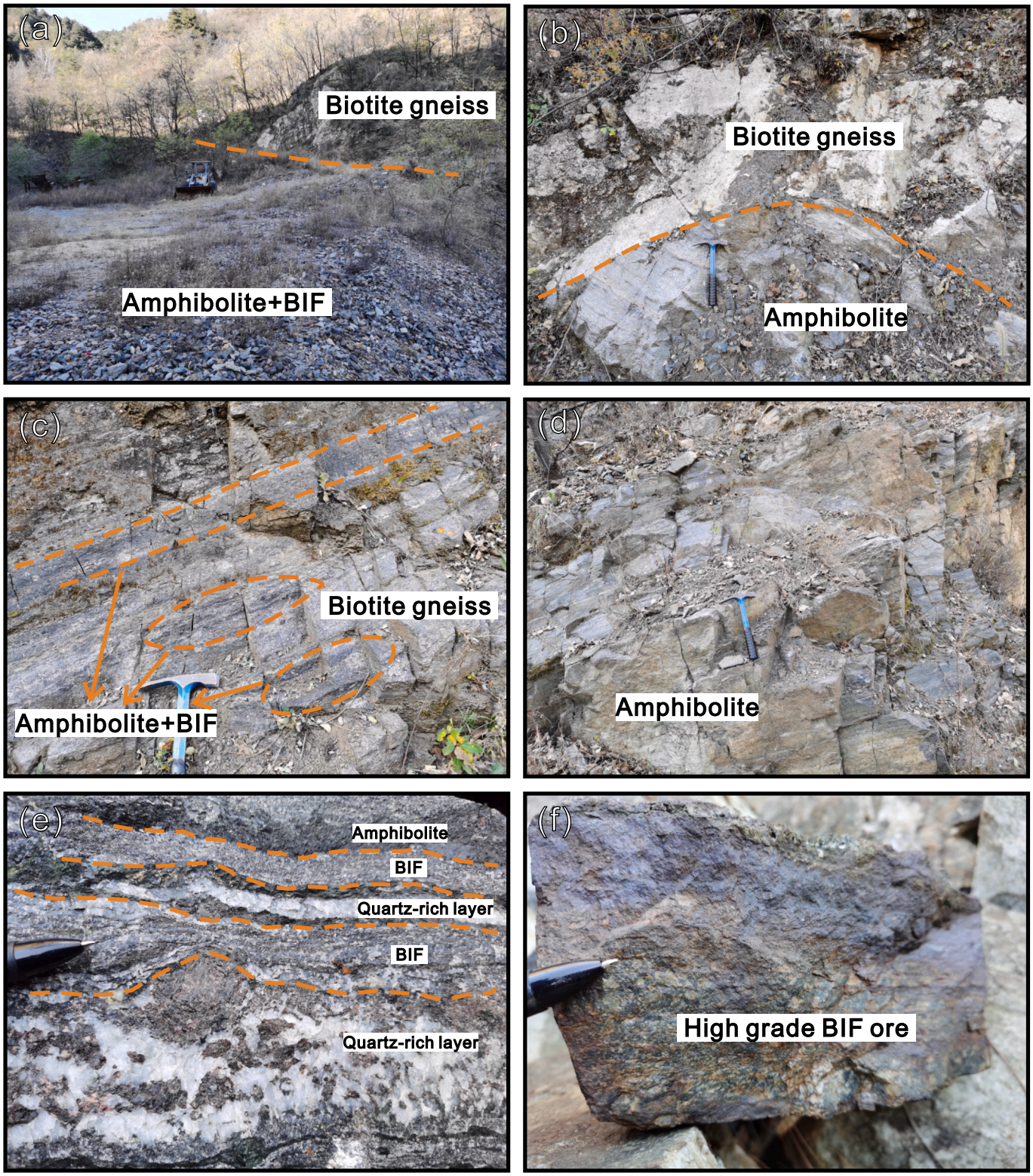

Fig. 3. Representative field photographs showing BIFs and associated rocks in the Fuping Complex. (a) Biotite gneiss and amphibolite + BIF; (b) contact between biotite gneiss and amphibolite; (c) amphibolite + BIF occur as thin layer and enclaves in biotite gneiss; (d) amphibolite; (e) interlayers of amphibolite and BIF with quartz-rich and quartz-poor portions; (f) high grade BIF ore.

4. Results

4.1. Petrography and mineralogy

The BIF samples 21FP-21B and 21FP-33 show russet color and are mainly composed of magnetite-rich and quartz-rich interlayers (Fig. 4d). The dominant metal minerals include magnetite (~30 vol%), pyrite (~2 vol%) and minor amounts of hematite (~1 vol%). The magnetite grains are anhedral to euhedral (5–500 μm), and coexist with hematite in some domains. Hematite occurs commonly in the oxidized ores and locally

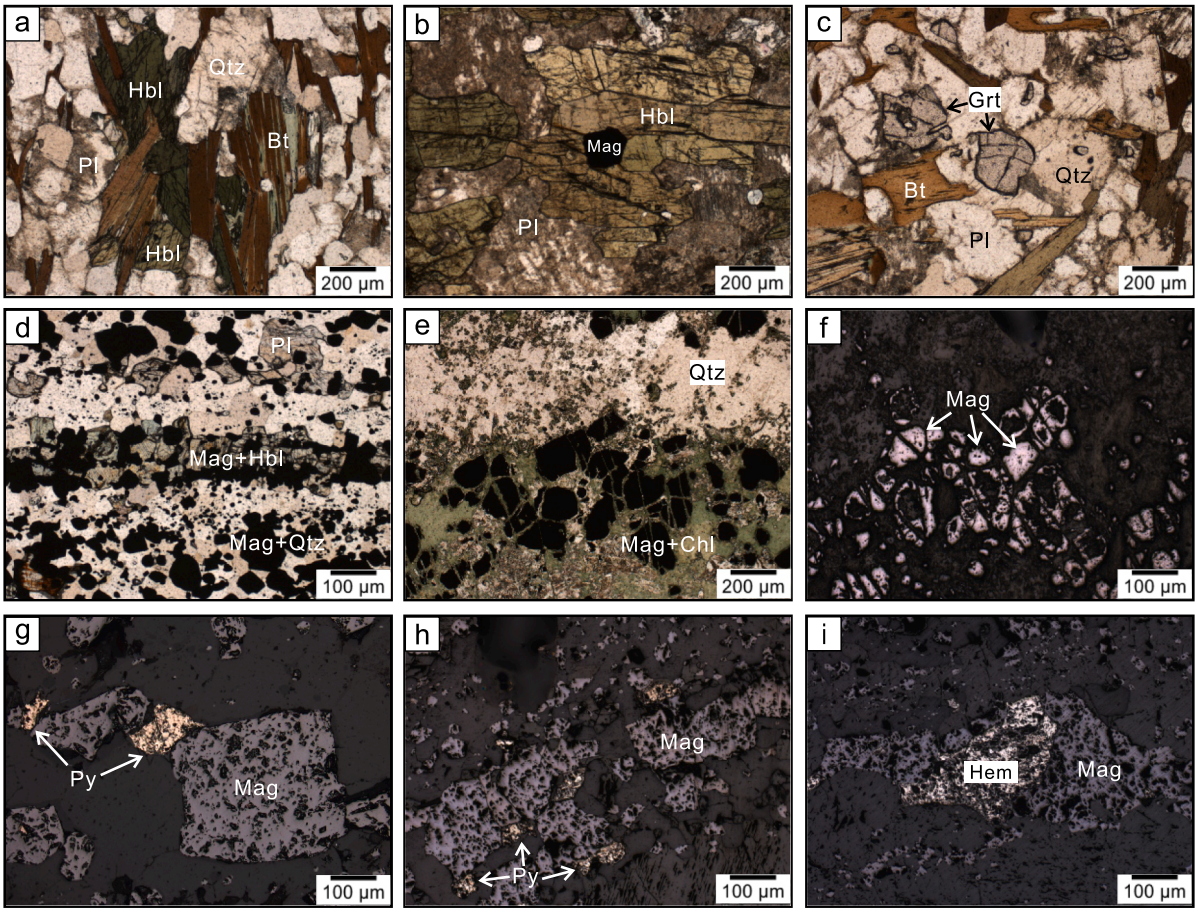

Fig. 4. Photomicrographs of BIF, amphibolite and biotite gneiss in the Fuping Complex. (a) Biotite gneiss (21FP-21A); (b) amphibolite sample 21FP-02, showing mineral assemblage of hornblende, plagioclase and magnetite; (c) biotite gneiss (21FP-36); (d) BIF ore with magnetite-rich and quartz-rich interlayers (21FP-21B); (e) BIF ore with quartz-rich band and chlorite + magnetite assemblage (21FP-30); (f) magnetite rich BIF ore (21FP-30); (g-h) magnetite and pyrite assemblage in BIF (21FP-33); (i) hematite and magnetite assemblage in BIF (21FP-21B). Mineral abbreviations: Hbl, hornblende; Pl, plagioclase; Qtz, quartz; Bt, biotite; Mag, magnetite; Chl, chlorite; Grt, garnet; Hem, hematite.

replace magnetite in primary ores (Fig. 4i). Pyrites are mainly fine-grained (1–10 μm) with few grains ranging in size of 50–100 μm (Fig. 4g-h). The gangue minerals consist of quartz (~50 vol%), hornblende (~12 vol%) and plagioclase (~5 vol%). Meanwhile, sample 21FP-30 consists of quartz (~40 vol%), magnetite (~30 vol%) and chlorite (~30 vol%). Quartz grains are mostly euhedral to subhedral, 1–2 mm in size and occur as quartz rich layers. Chlorites are light-green and commonly occur around or in the interstice of magnetite and quartz (Fig. 4e). Magnetite grains are anhedral to euhedral, showing grain size of 10–100 μm (Fig. 4f).

The amphibolite samples are typically dark-gray, medium- to coarse-grained, and exhibit moderate to weak foliation (Fig. 3e). The samples are composed dominantly of hornblende (~55 vol%), plagioclase (~25 vol%), quartz (~10 vol%), biotite (~5 vol%), garnet (<5 vol%) and magnetite (<5 vol%) (Fig. 4b). Anhedral to subhedral hornblende grains in most samples display weak orientation, spanning a variable grain size from 50 to 1500 μm. Plagioclases are commonly medium-grained (100–400 μm), euhedral to subhedral, and display sericitization occasionally (Fig. 4b). The quartz grains are subhedral to anhedral and mostly medium- to fine-grained (50–200 μm) with wavy extinction.

The biotite gneiss samples are dark greyish, medium- to coarse-grained and show gneissic structure. They consist mainly of quartz (~30 vol%), plagioclase (~30 vol%), hornblende (~15 vol%), biotite (~15 vol%) and minor amounts of garnet (~1 vol%) (Fig. 4a, c). The quartz grains are generally angular to subangular with 50–300 μm in size, but a minor portion of monocrystalline grains are spherical and well-rounded. Biotites often occur as tabular crystals varying in size from 50 to 300 μm, and show weak orientation. Minor chlorite occurs as alteration phase of biotite. Hornblendes are subhedral to euhedral, dark brown to light green with strong pleochroism and 100–400 μm in size.

4.2. Whole rock geochemistry

4.2.1. Amphibolite

The amphibolite samples have SiO_2 contents ranging from 48.26 wt % to 52.33 wt%, relatively high contents of alkalis (0.96–2.53 wt% K_2O and 2.82–3.78 wt% Na_2O) and CaO (4.91–10.09 wt%; Supplementary Table 2). The Al_2O_3 and $Fe_2O_3^T$ contents range from 13.12 wt% to 15.53 wt% and from 10.14 wt% to 16.11 wt%, respectively. The TiO_2 and MgO contents are relatively low, varying from 0.76 wt% to 1.35 wt% and from 4.84 wt% to 7.64 wt%, respectively. With respect to trace elements, all amphibolite samples show high LREE (e.g., La = 9.9–33.2 ppm, Ce = 15.7–70.8 ppm) and relatively low HREE (Tm = 0.295–0.452 ppm) (Fig. 5a) in the chondrite-normalized REE patterns (Sun and McDonough, 1989). In the primitive mantle-normalized trace element multi-element variation diagram (Fig. 5b), the amphibolites show enrichment of K, Rb, Ba, and depletion of Nb, Ta, Zr, U and Th.

4.2.2. Biotite gneiss

The biotite gneiss samples show limited variation of SiO_2 (59.63–61.23 wt%), Na_2O (2.97–3.39 wt%), K_2O (2.21–3.34 wt%) and Al_2O_3 (15.4–16.1 wt%) contents, moderate MgO (3.83–4.73 wt%) and

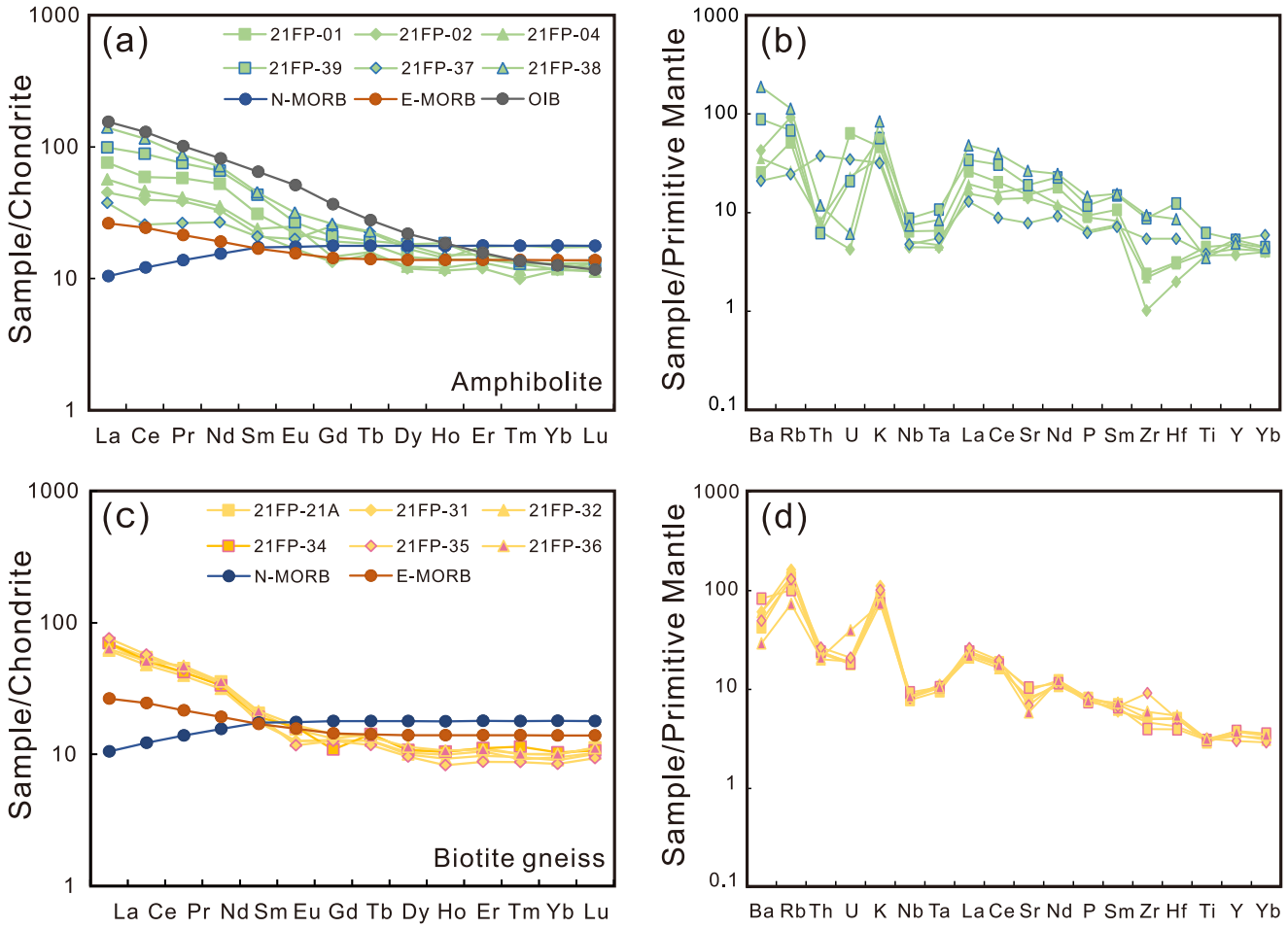

Fig. 5. Chondrite-normalized REE patterns (a, c) and primitive mantle-normalized trace element multi-element variation diagram (b, d) for the biotite gneisses and amphibolites from the Zhaigou deposit. The normalization values are from Sun and McDonough (1989).

$Fe_2O_3^T$ (7.03–8.14 wt%) contents, and relatively low TiO_2 (0.63–0.69 wt %), Cr (68.3–75.6 ppm) and Ni (34–39 ppm) contents (Supplementary Table 2), displaying distinct feature with Neoarchean TTG gneisses which have high SiO_2, Na_2O and low MgO contents (Liu and Yang, 2015). With respect to trace elements, all the biotite gneiss samples show high LREE contents (e.g., La = 14.5–18.0 ppm, Ce = 29.2–36.0 ppm) and Rb (46.4–103 ppm), but low HREE contents (Yb = 1.44–1.71 ppm). The chondrite-normalized REE patterns of biotite gneiss samples show significant LREE enrichment and HREE depletion (Fig. 5c). On the primitive mantle-normalized spider diagram, the HFSE such as Nb and Ta show notable depletions and the LILE (Rb, Ba, K) are strongly enriched (Fig. 5d).

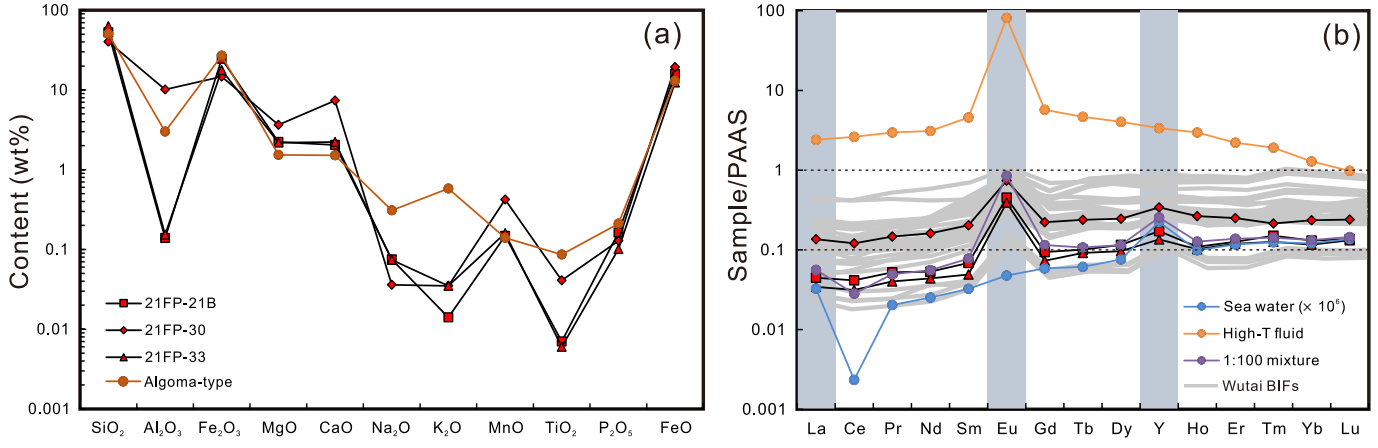

Fig. 6. (a) Major element contents of BIF samples, data of Algoma-type after Gross and Mcleod (1980). (b) PAAS-normalized REY patterns of BIF samples, showing the Wutai BIF data (Han et al., 2017; Wang et al., 2014), high-temperature (high-T) hydrothermal fluid of the Broken Spur vent in the mid-Atlantic ridge (Bau and Dulski, 1999), average values of modern North Pacific deep-sea water (Alibo and Nozaki, 1999) and modern surface seawater of south Pacific (Bolhar et al., 2004), and the 1:100 mixture of high-T hydrothermal fluid and average seawater.

4.2.3. BIF ore

The BIF samples are dominantly composed of SiO_2 (40.34–62.93 wt %) and $Fe_2O_3^T$ (30.16–40.34 wt%), with minor Al_2O_3, MgO, TiO_2 and CaO (Supplementary Table 2). In comparison with typical Algoma-type BIF ore (Gross, 1980), sample 21FP-30 has higher Al_2O_3 (10.1 wt%), CaO (7.36 wt%) and MnO_2 (0.423 wt%) contents (Fig. 6a). The BIF samples have relatively low trace element concentrations (ΣREE = 8.1–27.7 ppm), especially for incompatible elements such as Th (0.022–0.089 ppm), Hf (0.027–0.124 ppm), Zr (0.793–4.15 ppm) and Sc (0.175–1.41 ppm). The trace element characteristics can be reflected by the Post Archean Australian Shale (PAAS, McLennan, 1989) normalized REE and yttrium (REY) patterns. In the PAAS normalized REY diagram (Fig. 6b), the BIF samples show depletion of LREE relative to HREE with low $(La/Yb)_{PAAS}$ values (0.037–0.073), and exhibit positive Eu (3.34–6.21) and Pr (1.05–1.10) anomalies (Supplementary Table 2; Fig. 6b).

4.3. Zircon U–Pb geochronology

Three biotite gneiss samples (21FP-26B, 21FP-28B and 21FP-21A) and one BIF sample (21FP-21B) from the Zhaigou BIF deposit were used for LA-ICP-MS zircon U-Pb dating. The zircon U-Pb data are plotted in concordia diagrams (Figs. 7, 8) and listed in Supplementary Table 3, and zircon REE results are given in Supplementary Table 4.

4.3.1. Biotite gneiss

The zircon grains in biotite gneiss sample 21FP-26B are subhedral to anhedral, light brown to colorless and translucent. The zircon grains show near spherical morphology with size of 50–200 μm, and length to width ratios of 2:1 to 1:1. In CL images (Fig. 7a), the oscillatory zoning feature suggests igneous origin. A total of twenty-six spots were analyzed from twenty-six zircon grains (Fig. 7b). The dominant population shows $^{207}Pb/^{206}Pb$ ages from 2552 ± 30 Ma (Th/U = 0.19) to 2759 ± 31 Ma (Th/U = 0.61) with peak at ca. 2629 Ma (Fig. 7b). Four spots define another group with $^{207}Pb/^{206}Pb$ ages ranging from 2418 ± 66 Ma (Th/U = 0.31) to 2506 ± 55 Ma (Th/U = 0.70) and peak at ca. 2461 Ma. The remaining four grains define two groups with $^{207}Pb/^{206}Pb$ ages in the range of 2028 ± 26 Ma to 2075 ± 31 Ma, and 1846 ± 26 Ma to 1947 ± 28 Ma, representing the youngest detrital zircon ages of ca. 2.08–2.03 Ga and metamorphic ages of 1.95–1.85 Ga. The zircon trace elements display fractionated REE patterns with LREE depletion and HREE enrichment, and obvious Eu anomalies (Fig. 9a).

The zircons in sample 21FP-28B are subhedral to anhedral and well rounded. The near spherical grains are light brown to colorless and translucent with size of 60–200 μm, and length to width ratios of 2:1 to 1:1. In CL images, most zircons show core-rim textures or heterogeneous fractured domains and few zircons display oscillatory zoning (Fig. 7c). A total of twenty-six spots were analyzed from twenty-five zircon grains. The results define a major age population range between 2428 ± 35 Ma (Th/U = 0.61) and 2740 ± 28 Ma (Th/U = 0.75) with peak at ca. 2648 Ma. Three spots display $^{207}Pb/^{206}Pb$ ages from 2783 ± 36 Ma (Th/U = 0.84) to 2944 ± 38 Ma (Th/U = 0.36) (Fig. 7d). The zircon trace element results exhibit fractionated REE patterns with LREE depletion and HREE enrichment, and variable Eu anomalies (Fig. 9b).

Zircon grains in sample 21FP-21A are small (30–100 μm), translucent and colorless. The subhedral to anhedral grains show irregular or near spherical morphology with length to width ratios of 2:1 to 1:1. In CL images, most zircons are structureless, and some grains show core-rim texture with dark core and light bright rim (Fig. 7e). A total of seventeen spots were analyzed from seventeen zircon grains (Fig. 7f). All spots form a coherent group and fall along a Pb loss line, yielding weight mean $^{207}Pb/^{206}Pb$ age of 1831 ± 19 Ma (MSWD = 0.23) and an upper intercept age of 1875 ± 36 Ma (MSWD = 0.61) with Th/U ratios of 0.007–0.012. The zircon trace element results exhibit fractionated REE patterns with LREE depletion and HREE enrichment, and obvious negative Ce anomalies (Fig. 9c). Therefore, the ca. 1.83 Ga age is taken to represent the metamorphic age of the biotite gneiss.

4.3.2. BIF ore

Zircon grains in BIF sample 21FP-21B are euhedral to subhedral and exhibit short prismatic or irregular morphology, light brown to colorless, and translucent. The grain sizes range from 50 μm to 150 μm and show length to width ratios of 1.5:1 to 1:1. In CL images, most zircons are structureless, and some grains show core-rim texture with light core and dark rim (Fig. 8a). A total of twenty-two spots were analyzed from twenty-two zircon grains (Fig. 8b). Fourteen spots on the heterogeneous fractured domains are distributed along a Pb loss line and yield weighted mean $^{207}Pb/^{206}Pb$ age of 2028 ± 33 Ma (MSWD = 0.094). Eight spots on the rim domains form another group near the concordia, yielding an upper intercept age of 1874 ± 52 Ma (MSWD = 0.09), with Th/U ratios ranging from 0.004 to 0.2. The zircon trace element data show fractionated REE patterns with LREE depletion and HREE enrichment, and variable Eu anomalies (Fig. 9d). Therefore, the 2028 Ma age obtained from heterogeneous fractured domains is interpreted to represent the mineralization age of the BIF ore, followed by metamorphism at ca. 1874 Ma.

4.4. Major and trace elements of magnetite

Major and trace elements compositions of magnetite in BIF samples are provided in Supplementary Table 5. Magnetites are Fe-rich (average $Fe_2O_3^T$ = 90.9–92.3 wt%). Compared with magnetite of typical BIFs around the world (Dupuis and Beaudoin, 2011), magnetites in 21FP-21B and 21FP-33 are depleted in TiO_2 (0.001–0.003 wt%), CaO (0.003–0.015 wt%) and Al_2O_3 (0.073–0.279 wt%). Magnetites in samples 21FP-21B and 21FP-33 have higher MnO (0.06–0.083 wt%) and MgO (0.02–0.05 wt%) contents and lower TiO_2, Al_2O_3, CaO and Na_2O contents than those in sample 21FP-30 (Fig. 10 a-f). With respect to trace elements, the contents of V and Cr in magnetite from 21FP-21B and 21FP-33 are extremely low (<5 ppm), the magnetites from 21FP-30 are enriched in Co, Ga, Mo and Sn.

5. Discussion

5.1. Formation age of the BIF deposit

The BIF deposits in China were mainly formed in the Neoarchean with subordinate deposits during the Paleo, *Meso* and Neoproterozoic time (Li et al., 2014; Dai et al., 2016). The Neoarchean BIFs are mainly Algoma-type, with a minor group of Paleoproterozoic and Mesoproterozoic BIF deposits belonging to Superior-type (Li et al., 2014). The Zhaigou BIF ores in the Fuping Complex are closely associated with biotite gneiss and amphibolite in the Wanzi supracrustal sequence (Fig. 2). In this study, we obtained weighted mean ages of 2028 ± 33 Ma and 1874 ± 52 Ma from the BIF ores (Fig. 8b). The former age group was obtained from heterogeneous fractured domains as identified in CL image, and the corresponding zircon trace elements show a steep left-dipping curve with apparently positive Ce and partially negative Eu anomalies in the chondrite-normalized REE patterns, indicating that the BIF ore was related to the ca. 2.03 Ga magmatic activity. Notably, available zircon U–Pb age data suggested that the protolith of the amphibolite in the Fuping Complex was crystallized at 2.1–2.0 Ga in subduction related arc setting (Tang et al., 2015). Furthermore, the Wanzi supracrustal sequence hosting the Zhaigou BIF deposit is considered to have deposited in Paleoproterozoic. Ren et al. (2013) reported detrital zircon ages of quartzite and proposed that the deposition age for the protolith was before 2.1–2.0 Ga and after 2.5 Ga. Xia et al. (2006) suggested that the supracrustal assemblage was deposited between 2.10 and 1.84 Ga by the youngest detrital zircon age and the metamorphic age of the metasedimentary rocks. The youngest detrital zircon U–Pb age group from biotite gneiss sample (Fig. 7b) displays concordant age in a range of 2028 ± 26 Ma to 2075 ± 31 Ma, which

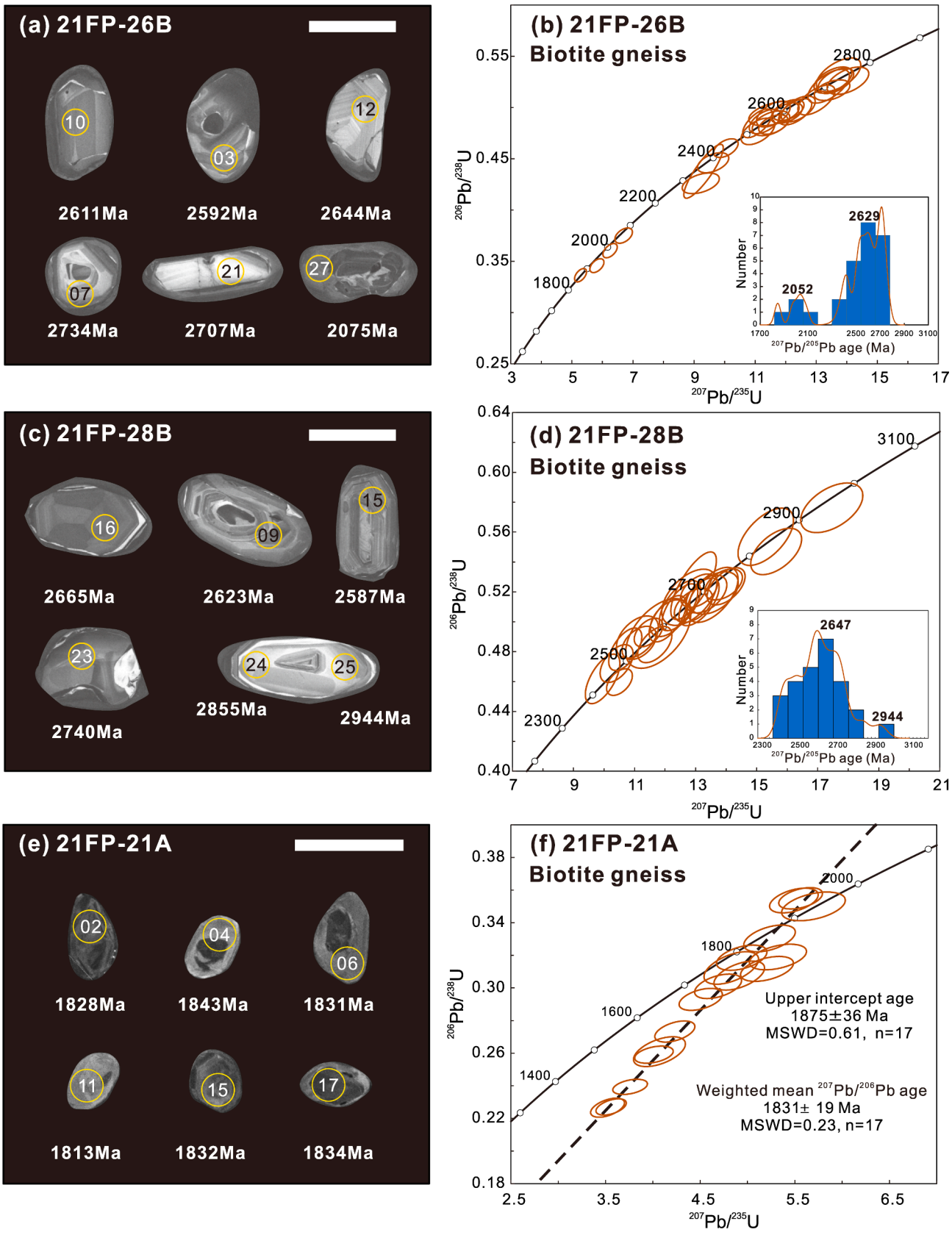

Fig. 7. Representative CL images (a, c, e) of zircons and concordia plots (b, d, f) of the biotite gneiss samples (21FP-26B, 21FP-28B and 21FP-21A). Scale bars are 100 μm.

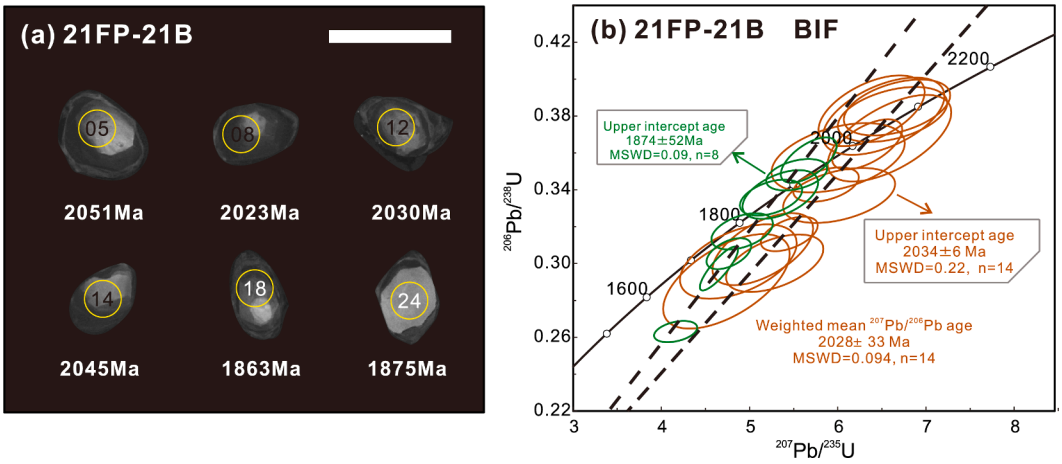

Fig. 8. Representative CL images (a) of zircons and concordia plots (b) of the BIF ore (21FP-21B). Scale bars are 100 μm.

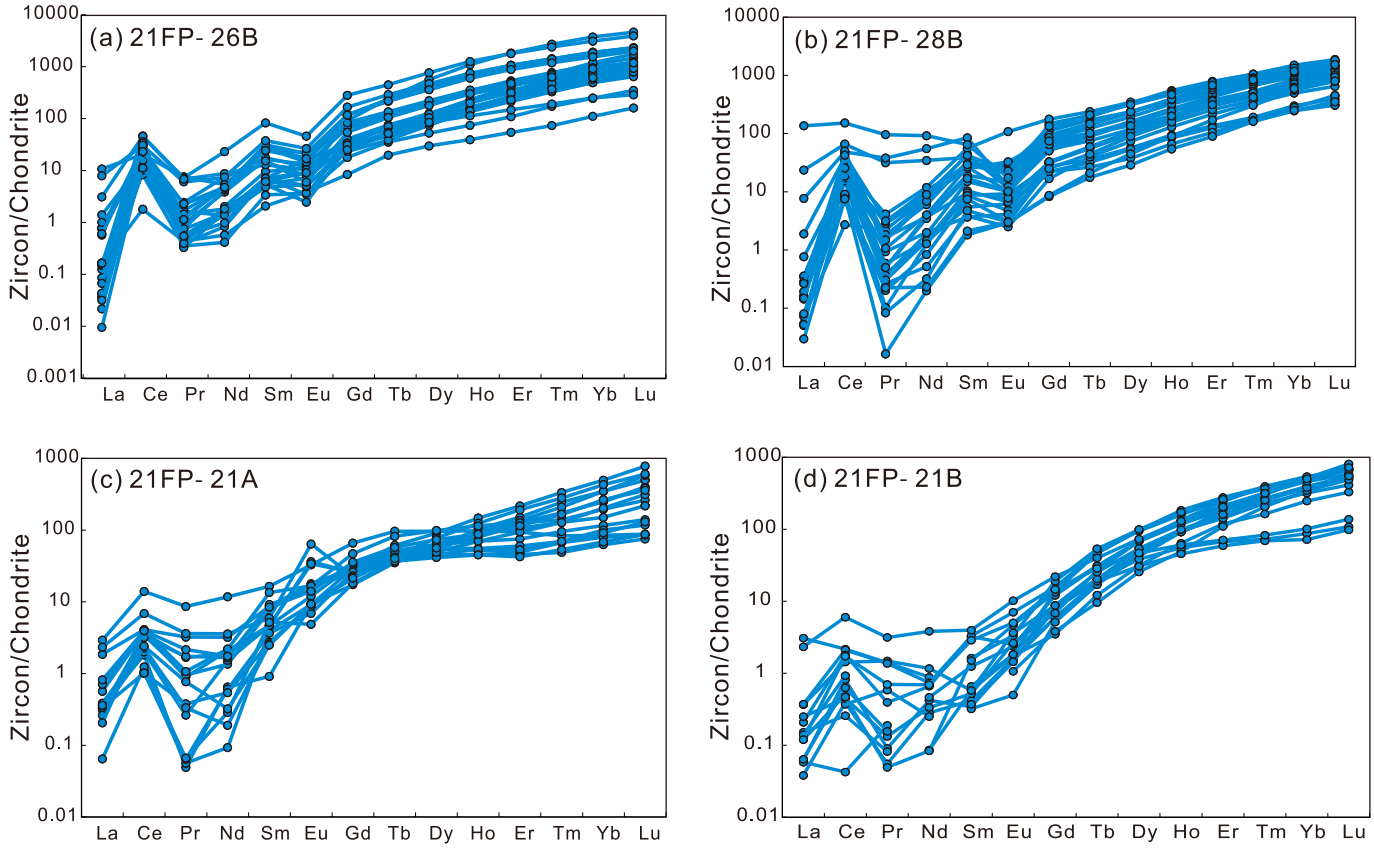

Fig. 9. Chondrite-normalized REE patterns of zircons in samples 21FP-26B (a), 21FP-28B (b), 21FP-21A (c) and 21FP-21B (d).

further constrains the depositional age as approximately after 2.03 Ga for the Wanzi supracrustal sequence. Thus, the depositional age of the Zhaigou BIF deposit is considered as 2028 ± 33 Ma which is consist with the age of basaltic magmatism and Wanzi supracrustal deposition in the FPC, and then underwent a subsequent metamorphic event at 1874 ± 52 Ma. In addition, Huston and Logan (2004) compared the Eu/Eu^*_{NASC} ratios in BIFs and identified the relatively higher Eu/Eu^*_{NASC} ratios (>1.8) in Algoma-type BIFs. In this study, the Eu/Eu^*_{NASC} ratios of the Zhaigou BIF ores are 3.79–7.01, in combination with the close association between BIF, amphibolite and biotite gneiss, indicating the affinity of Algoma-type BIF deposit. Therefore, the Zhaigou Algoma-type BIF deposit and the associated metabasaltic and *meta*-sedimentary rocks are the product of the same volcanic-sedimentary event during 2.1–2.0 Ga (Tang et al., 2015).

The Paleoproterozoic depositional age of the Zhaigou BIF deposit is obviously younger than the large-scale BIF deposition event (2.55–2.50 Ga) in the NCC (Fig. 1). The Neoarchean BIF deposits are widely distributed in the NCC, such as the Waitoushan BIF (2533 Ma, Dai et al., 2012), Gongchangling BIF (2539 Ma, Li et al., 2016), Nanfen BIF (2552 Ma, Zhu et al., 2015) in the Anshan-Benxi area, Malanzhuang BIF (2545 Ma, Li et al., 2015) and Shuichang BIF (2536 Ma, Han et al., 2014) in the Zunhua area, Wangjiazhuang BIF (2543 Ma, Wang et al., 2014) and Baiyuli BIF (2543 Ma, Han et al., 2017) in the Wutai area, and Dengfeng BIF (2534 Ma, Huang et al., 2019) and Xincai BIF (2680 ~ 2488 Ma, Lan et al., 2019) in the southern segment of the NCC. Most of them are hosted in greenschist- to lower amphibolite-facies *meta*-volcanic rocks

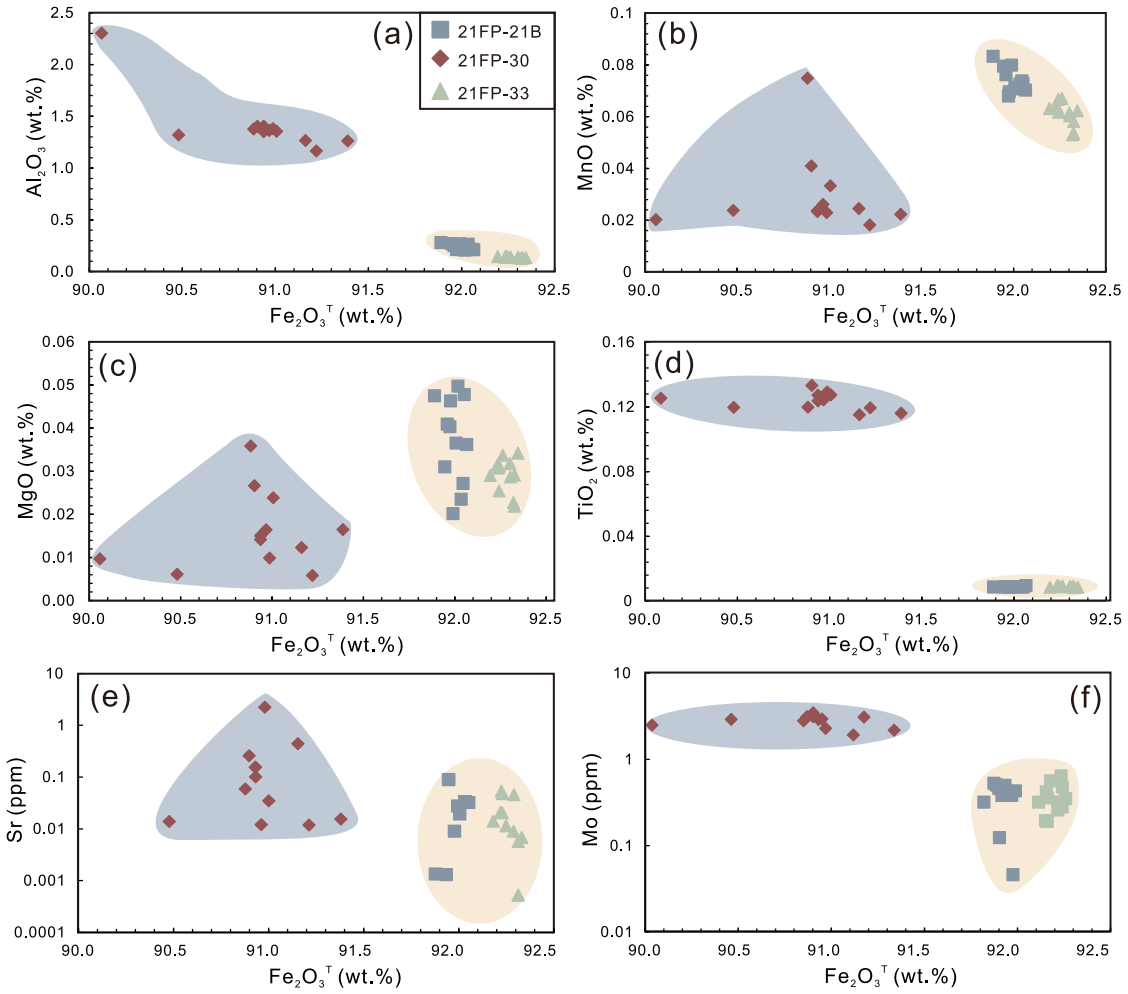

Fig. 10. Binary diagrams of magnetite in BIF ores from the Zhaigou deposit.

and pyroclastic rocks, and belong to Algoma-type (Zhai and Santosh, 2013; Li et al., 2014). The late Neoarchean volcanic and hydrothermal activities were correlated with the microblock amalgamation process which brought volcanic and terrigenous inputs, and resulted in the BIF deposition in arc-related basins (Manikyamba et al., 1993; Zhai and Santosh, 2011, 2013; Tang and Santosh, 2018b). Besides, a small number of BIF deposits in the NCC were formed in the Paleoproterozoic (e.g. Yuanjiacun iron deposit; Wang et al., 2015), Mesoproterozoic (e.g. Jingtieshan iron deposit; Sun et al., 1998) and Neoproterozoic (e.g. Xinyu iron deposit and Shilu iron deposit; Li et al., 2014). The Paleoproterozoic BIFs in the Lüliang Complex (Yuanjiacun iron deposit) and Luxi area (Changyi iron deposit) are associated with marine clastic–carbonate sedimentary formations and thought to be Superior-type (Li et al., 2014). Lan et al (2014a, 2014b) proposed that the Changyi Superior-type BIF deposit was formed at 2.24–2.19 Ga in a continental rift environment. However, the Zhaigou BIF deposit belongs to Algoma-type which is evidenced by the lithology of BIF and amphibolite (*meta*-basalt; Fig. 3c and e), and high Eu/Eu^*_{NASC} ratios (3.79–7.01, Supplementary Table 2), representing a newly discovered Paleoproterozoic Algoma-type BIF deposit in the central NCC.

5.2. Origin and source characteristics of the BIF deposit

As Al_2O_3 and TiO_2 cannot be introduced by solution, their concentrations are commonly used to trace the degree of contamination of terrigenous detrital materials in BIFs (Pecoits et al., 2009). The Zhaigou BIF samples 21FP-21B and 21FP-33 are dominantly composed of SiO_2 (52.7–62.9 wt%) and $Fe_2O_3^T$ (40.3–30.2 wt%), and have relatively low contents of Al_2O_3 (0.139–0.153 wt%), TiO_2 (<0.01 wt%), and HFSEs (Zr, Hf, Th, and U) (Supplementary Table 2). In contrast, the BIF sample 21FP-30 is characterized by aluminum-rich minerals and has higher contents of Al_2O_3, TiO_2 and HFSEs. In combination with the close spatial relationship with biotite gneisses which show detrital zircon age population of 2.76–2.46 Ga, we propose significant contribution of Neoarchean continental crust such as the Fuping TTG gneisses and contemporary mafic–ultramafic rocks (Tang et al., 2016) in the provenance. Furthermore, continental crust is enriched in Sr, Al, Ti and Mo (Rudnick and Fountain, 1995), and is the dominant source for dissolved Sr in seawater (Pecoits et al., 2009). Magnetites in 21FP-30 have relatively high concentrations of Sr, Al, Ti and Mo (Fig. 10) which also indicate the contribution of terrigenous detrital material during BIF deposition.

The typical BIFs have similar REY patterns with modern seawater which usually shows HREE enrichment, positive La and Y anomalies, and higher Y/Ho ratios than chondrites (German et al., 1995; Alibo and Nozaki, 1999; Bau and Dulski, 1996). The PAAS normalized REY patterns of the Zhaigou BIFs display LREE depletion, positive La, Eu, and Y anomalies which are consistent with the Neoarchean BIFs in the Wutai Complex (Han et al., 2017; Wang et al., 2014). The REY distribution patterns of the Zhaigou BIFs are similar to the 1:100 mixture of high-temperature hydrothermal fluid and seawater (Fig. 6b). In addition, the strongly positive Eu anomalies of the Zhaigou BIF samples are also consistent with the typical feature of submarine high-temperature hydrothermal fluids (Bau and Dulski, 1999), suggesting the involvement of

high-temperature hydrothermal fluids in the deposition of the BIF ore. The SiO_2-Al_2O_3 and (Co + Ni + Cu)-REY diagrams also indicate that the BIF deposit has a genetic link with submarine hydrothermal activity (Manikyamba et al., 1993; Fig. 11a and b). Concentrations of Cu, Co, Ni, Zn, and Pb can also reflect the contribution of hydrothermal fluid (Sugitani, 1992). In the total REE versus Co + Ni + Cu diagram (Fig. 11b), all the Zhaigou BIF samples plot close to the field of deep-sea hydrothermal deposits, suggesting that the enriched transition metals (e.g., Ni, Zn) could be derived from the submarine hydrothermal activities.

In summary, the Zhaigou BIF deposit might have been contributed by high-temperature hydrothermal fluids, sea-water, and terrigenous component. As the positive Eu anomalies of BIF can only reflect the temperature of the hydrothermal system but cannot be used for mass fraction calculations regarding the mixture of high-temperature hydrothermal fluids and seawater (Bau and Möller, 1993), and considering REY patterns of terrigenous materials input, Alexander (2008) proposed two-component mixing models using Sm/Yb versus Y/Ho (Fig. 12a) and Eu/Sm versus Sm/Yb ratios (Fig. 12b) of modern shallow seawater (Alibo and Nozaki, 1999) and high-temperature hydrothermal fluids (Bau and Dulski, 1999). Here we use the end-member mixing model of seawater (Alibo and Nozaki, 1999), high-temperature hydrothermal fluids (Bau and Dulski, 1999) and TTG rocks (Tang et al., 2016). According to the modeling results (Fig. 12), the mixing of minor high-temperature hydrothermal fluid (0.1 % ~ 1 %) with seawater can explain the Sm/Yb and Eu/Sm ratios of the Zhaigou BIFs, whereas the Neoarchean BIFs in the Wutai Complex show less contribution of high-temperature hydrothermal fluid (<0.1 %). However, the additional REY sources (e.g., crustal fluxes) and the existing differences between modern end-member components and those of local conditions in the Archean may lead to the relatively low Y/Ho ratios (Alexander et al., 2008; Huang et al., 2019). The Y/Ho ratios (~38) of the Zhaigou BIF ores fall between those of hydrothermal fluids (26–28), terrestrial materials (~26) and modern seawater (>44) (Bau and Dulski, 1996; Bolhar et al., 2004). Based on the distribution of BIF samples along with the TTG gneiss (Fig. 12a), we suggest that the terrigenous detrital materials were probably derived from TTG rocks. The dominant group of detrital zircons with Archean ages (2.76–2.46 Ga; Fig. 7b, d) also suggests the provenance from the Fuping TTG gneiss. Tang et al. (2015) proposed that the Wanzi supracrustal sequences was sourced from the Fuping TTG gneisses. Therefore, the Zhaigou BIF deposit is considered as the product of mixtures of seawater and high-temperature hydrothermal fluids with minor terrestrial input from TTG gneisses in a submarine environment.

5.3. Redox state of the Paleoproterozoic seawater

The Ce^{3+} can be oxidized to Ce^{4+} which decreases the solubility of Ce in the oxidizing environment, resulting in its preferential removal onto suspended particles in seawater (e.g., Mn-Fe oxyhydroxides, organic matter, and clay particles), and then leading to a strong negative Ce anomaly in oxygenated modern seawater and decoupled Ce from other REEs (Alibo and Nozaki, 1999; Planavsky et al., 2010). The Ce anomaly is widely used for estimating the redox state during the formation of BIFs in oceanic basins (German and Elderfield, 1990). In the Pr/Pr* versus Ce/Ce* diagram (Fig. 13), the Zhaigou BIF samples plot mainly in the fields of no Ce anomaly to negative Ce anomaly, indicating that the Paleoproterozoic Zhaigou BIF deposit was formed in oxidized condition. In addition, the Th-U decoupling can be employed to qualitatively constrain the oxidation levels (Bau and Alexander, 2009). Decoupling of Th and U is commonly attributed to oxidation of immobile U^{4+} to mobile U^{6+} during oxic weathering or diagenesis, eventually resulting in lower Th/U ratio in seawater (Collerson and Kamber, 1999). The fractionated Th/U ratios (0.39–7.33) observed in the Zhaigou BIF ores suggest that the ambient ocean had received preferential U input, indicating mildly oxidizing conditions in the source area. However, numerous studies have shown that most Neoarchean BIFs in the NCC and worldwide show the lack of Ce anomaly, variable Y/Ho and LREE/HREE ratios before the Great Oxygenation Event (GOE, Bau and Dulski, 1996; Bekker et al., 2010; Planavsky et al., 2010; Konhauser et al., 2017; Huang et al., 2019). Lan et al. (2014) identified obvious negative Ce anomaly in the Paleoproterozoic Changyi BIF (2240–2193 Ma) in the eastern part of the NCC, and proposed that the deposition process was influenced by the GOE (2.45–2.22 Ga, Bekker et al., 2004). Therefore, we infer that the seawater during the deposition of the Zhaigou BIFs was oxidized after the GOE in Paleoproterozoic.

5.4. Tectonic setting for the formation of the Zhaigou BIF deposit

The formation of the Zhaigou BIF deposit and the associated amphibolite represents an important volcanic-hydrothermal event during 2.1–2.0 Ga when widespread magmatic events occurred in the various complexes in the TNCO (Tang et al., 2015). The amphibolite samples are classified as subalkaline basalt in the Zr/TiO_2 versus Nb/Y diagram (Fig. 14a; Pearce, 1996). In the Ti versus Zr diagram, amphibolite samples fall in the field of volcanic arc basalt (Fig. 14b; Pearce, 1996). Furthermore, they show affinity with calc-alkaline basalt and island arc tholeiite in the MnO_2-TiO_2-P_2O_5 diagram (Fig. 14c; Mullen, 1983). The amphibolites from the Zhaigou deposit display

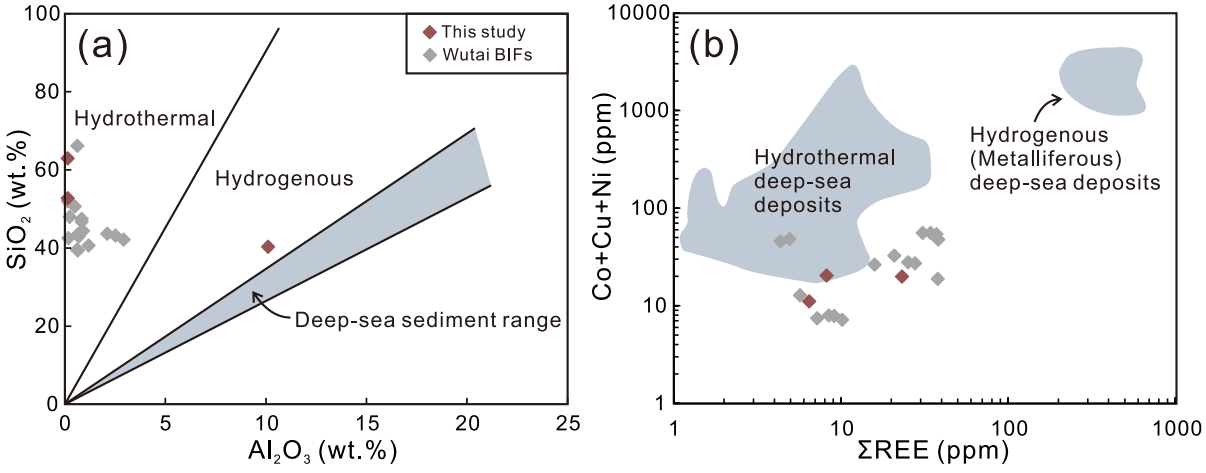

Fig. 11. Al_2O_3-SiO_2 diagram illustrating hydrothermal fluids may have provided the iron for the Zhaigou BIF (after Wonder et al., 1988). (b) (Co + Cu + Ni) – ΣREE diagram (after Dymek and Klein, 1988) showing most samples within or very close to the field of hydrothermal deposits. Data of the Wutai BIFs from Zhaocun and Sanyangping iron deposit are from Han et al. (2017).

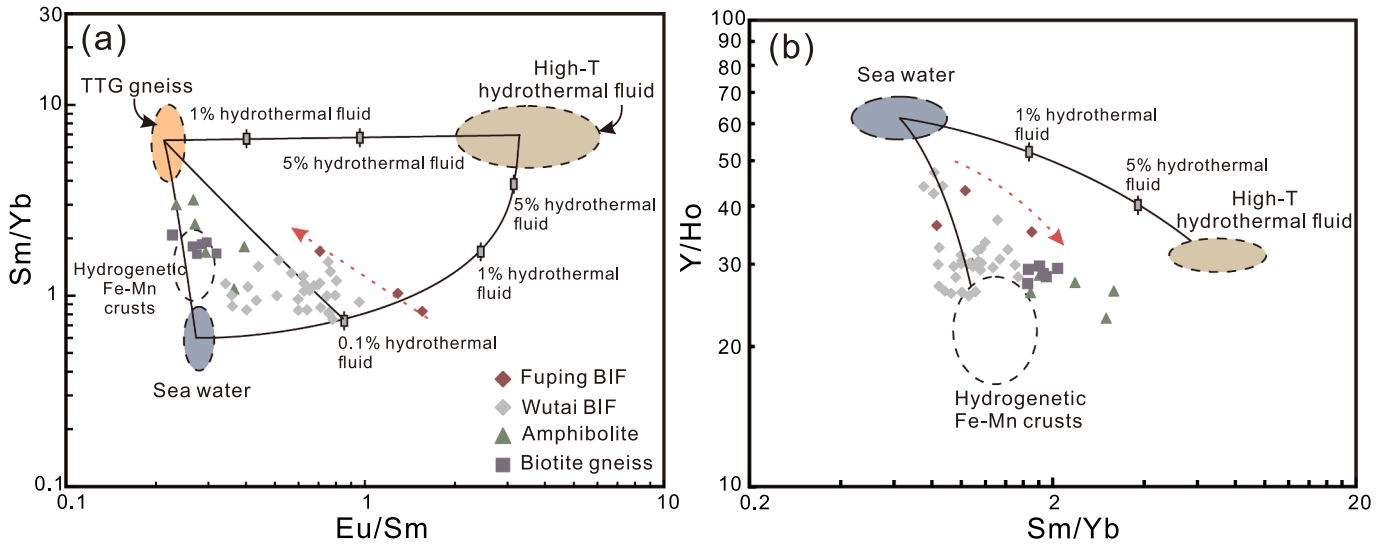

Fig. 12. Elemental mixing models using Y/Ho, Sm/Yb and Eu/Sm ratios of modern shallow seawater (Alibo and Nozaki, 1999) and high-temperature hydrothermal fluids from the Mid-Atlantic Ridge (>350 °C) (Bau and Dulski, 1999) to evaluate the relative proportions of fluid contributions to the REY distribution in BIFs (Alexander et al., 2008). (a) Eu/Sm versus Sm/Yb diagram shows that minor contribution (0.1 %-1%) of high-T hydrothermal fluid for the Zhaigou BIFs. (b) Sm/Yb versus Y/Ho disgram shows that the involvement of minor high-T hydrothermal fluid (<1%) for the Zhaigou BIFs. Data of the BIFs in the Wutai greenstone belt are from Wang et al. (2014) and Han et al. (2017).

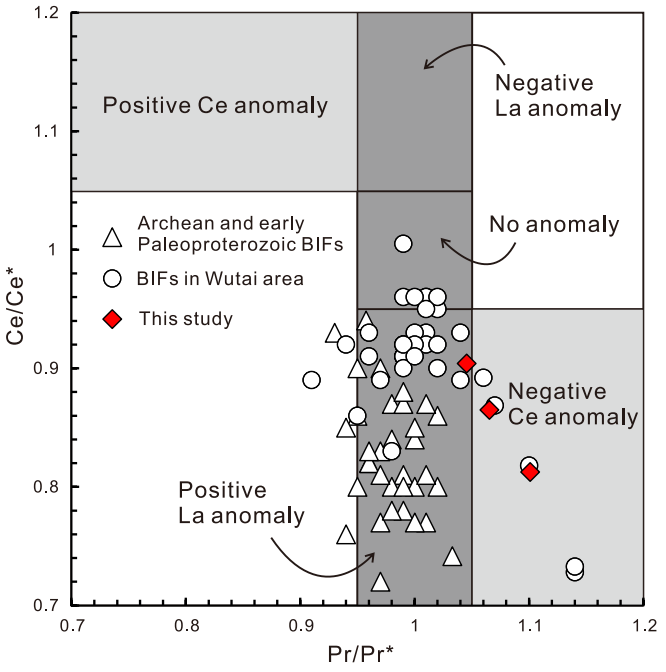

Fig. 13. Ce/Ce*-Pr/Pr* discrimination diagram for Ce anomaly (after Bau and Dulski, 1996).

relatively low Th/Ta ratios (1.20–14.2) which are consistent with the characteristic of island arc basalts (Fitton et al., 1991). In addition, the Th/Yb versus Ta/Yb diagram (Fig. 14d; Pearce, 1982) and chondrite-normalized REE patterns (Fig. 5a) also suggest that the amphibolite samples have ocean island arc affinity. Notably, the 2.1–2.0 Ga granitic and metabasaltic magmatism in the Fuping Complex and TNCO were considered to have been formed in subduction-related arc setting (Santosh et al., 2015) or intra-plate rift setting (Zhang et al., 2011; Peng et al., 2012; Wang et al., 2020). Tang et al. (2015) summarized the 2.1–2.0 Ga granitic and *meta*-basaltic rocks in the TNCO and proposed a double-sided subduction model with subduction process in the Fuping Complex forming the Nanying granitic gneiss and *meta*-basalt. Therefore, the Zhaigou BIFs and protolith of the 2.1–2.0 Ga amphibolite were formed in an oceanic basin related to island arc setting during the Paleoproterozoic terrane assembly process along the TNCO.

Algoma-type BIFs are generally formed in stable semi-deep to deep water environment in island arc or back-arc basin (Veizer, 1983). Submarine volcanism and hydrothermal vents can provide metal-rich high-temperature hydrothermal fluids (Manikyamba et al., 1993; Huang et al., 2019). As discussed above, the divergent double subduction of the oceanic lithosphere resulted in distinct 2.1–2.0 Ga arc magmatism in the Fuping Complex. In the oceanic basin related to island arc environment, the metal-rich high-temperature fluids were generated from deep sea vents which were closely related to submarine basaltic magmatism. The mixture of high-temperature hydrothermal fluids and sea water, in combination with significant terrigenous inputs, resulted in the formation of the Zhaigou BIF ores and the associated *meta*-basalt and *meta*-sedimentary sequence in oxidized seawater environment.

6. Conclusions

(1) The Zhaigou BIF deposit belongs to the Algoma-type which shows close association with the Paleoproterozoic sedimentary sequence and amphibolite. Zircon U-Pb data constrain the formation of BIF ore and a later metamorphic event at ca. 2.03 Ga and 1.87–1.83 Ga, respectively.

(2) The Zhaigou BIF deposit is considered as the product of mixtures of seawater and high-temperature hydrothermal fluids (0.1 %~1%) with terrestrial materials input from TTG gneisses in an oxic submarine environment.

(3) The Paleoproterozoic seawater for the formation of the Zhaigou BIF was oxidized after the GOE.

(4) The Zhaigou BIF was formed in the island arc related oceanic basin during the Paleoproterozoic terrane assembly within the TNCO.

Declaration of Competing Interest

The authors declare that they have no known competing financial interests or personal relationships that could have appeared to influence the work reported in this paper.

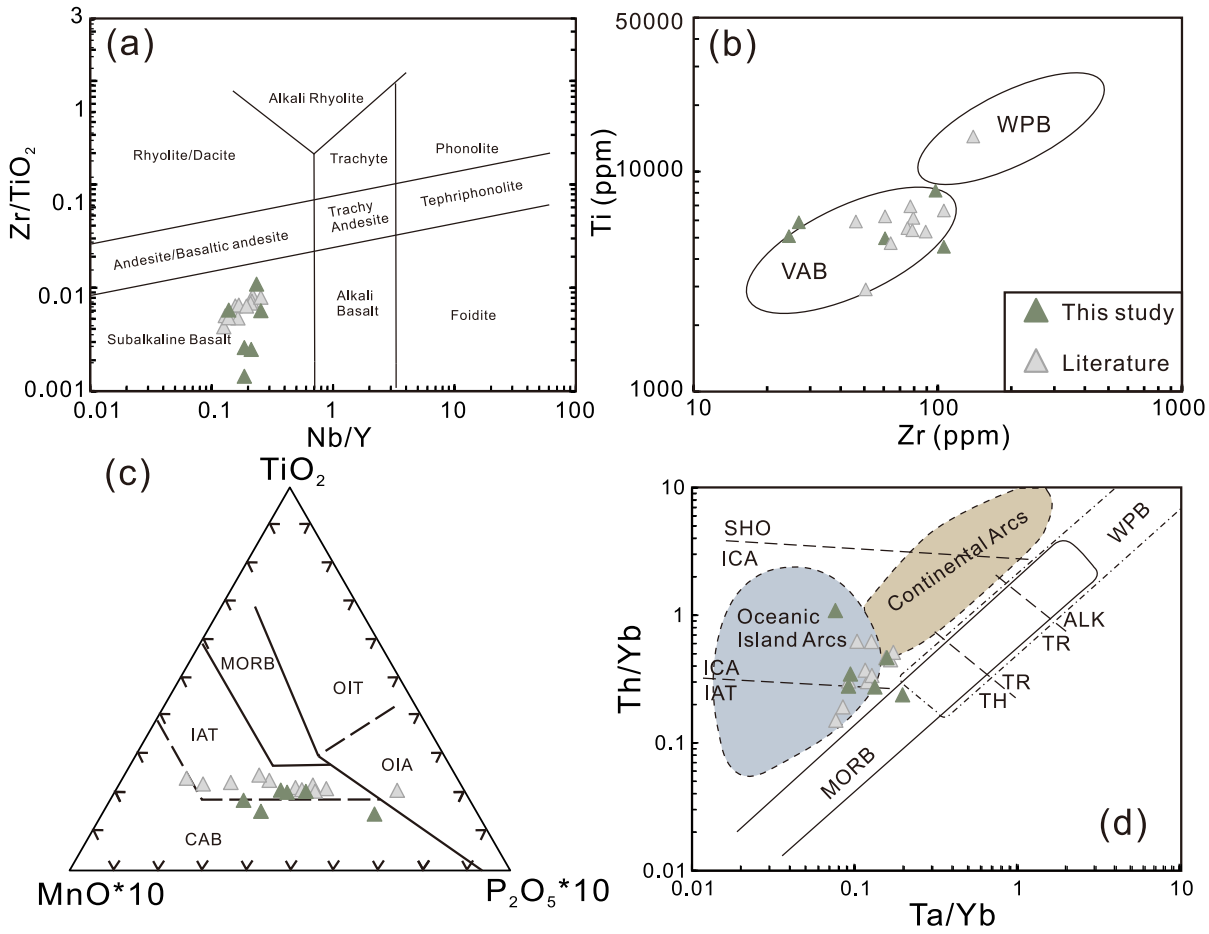

Fig. 14. Diagrams showing compositions and protolith reconstruction of amphibolites from the Fuping Complex. Amphibolite data from this study (green) and literature (grey; Tang et al. (2015)). (a) Zr/TiO_2 versus Nb/Y classification diagram and (b) Ti–Zr discrimination diagram, WPB: within-plate basalt, VAB: volcanicarc basalt (Pearce, 1996). (c) Plots of MnO*10-TiO_2-P_2O_5*10, CAB: cal-alkaline basalt; IAT: island arc tholeiite; OIT: ocean island tholeiite; OIA: ocean island alkalic basalt (Mullen, 1983). (d) Th/Yb versus Ta/Yb diagram, IAT: island arc tholeiite; ICA: island arc calc-alkali basalt; SHO: island arc shoshonite; WPB: within plate basalt; TH: tholeiite series; TR: transitional series; ALK: alkaline series (Pearce, 1982).

Data availability

All data are available in supplementary tables

Acknowledgements

We are grateful to Prof. Huayong Chen (Editor-in-Chief) and two anonymous reviewers for their constructive comments and suggestions. We thank Xin-Kai Hu, Yuan-Ming Sheng, Jia-Ying Feng, Pei-Lin Chen, Peng Xiang and Jia-Lin Wang for their help in the field and analytical works. This study was jointly supported through the Open Research Project from the Key Laboratory of Tectonic Controlled Mineralization and Oil Reservoir of Ministry of Natural Resources (gzck202103) and National Natural Science Foundation of China (41902193).

Appendix A. Supplementary data

Supplementary data to this article can be found online at https://doi.org/10.1016/j.oregeorev.2023.105314.

References

Alexander, B.W., Bau, M., Andersson, P., Dulski, P., 2008. Continentally derived solutes in shallow Archean seawater: rare earth element and Nd isotope evidence in iron formation from the 2.9 Ga Pongola Supergroup. South Africa. Geochim. Cosmochim. Acta 72, 378–394.

Alibo, D.S., Nozaki, Y., 1999. Rare earth elements in seawater: particle association, shale normalization, and Ce oxidation. Geochim. Cosmochim. Acta 63, 363–372.

Bai, J., Huang, X., Wang, H., 1996. The Precambrian Crustal Evolution of China. Geol. Publ. House, Beijing 1–259 in Chinese with English abstract.

Bau, M., Alexander, B.W., 2009. Distribution of high field strength elements (Y, Zr, REE, Hf, Ta, Th, U) in adjacent magnetite and chert bands and in reference standards FeR-3 and FeR-4 from the Temagami iron-formation, Canada, and the redox level of the Neoarchean ocean. Precambrian Res. 174, 337–346.

Bau, M., Dulski, P., 1996. Distribution of yttrium and rare-earth elements in the Penge and Kuruman iron-formations, Transvaal Supergroup. South Africa. Precambrian Res. 79, 37–55.

Bau, M., Dulski, P., 1999. Comparing yttrium and rare earths in hydrothermal fluids from the Mid-Atlantic Ridge: implications for Y and REE behaviour during near-vent mixing and for the Y/Ho ratio of Proterozoic seawater. Chem. Geol. 155, 77–90.

Bau, M., Möller, P., 1993. Rare earth element systematics of the chemically precipitated component in early Precambrian iron formations and the evolution of the terrestrial atmosphere–hydrosphere–lithosphere system. Geochim. Cosmochim. Acta 57, 2239–2249.

Bekker, A., Holland, H.D., Wang, P.L., Rumble III, D., Stein, H.J., Hannah, J.L., Coetzee, L.L., Beukes, N.J., 2004. Dating the rise of atmospheric oxygen. Nature 427, 117–120.

Bekker, A., Slack, J.F., Planavsky, N., Krapez, B., Hofmann, A., Konhauser, K.O., Rouxel, O.J., 2010. Iron Formation: The Sedimentary Product of a Complex Interplay among Mantle, Tectonic, Oceanic, and Biospheric Processes. Econ. Geol. 105, 467–508.

Bolhar, R., Kamber, B.S., Moorbath, S., Fedo, C.M., Whitehouse, M.J., 2004. Characterisation of early Archaean chemical sediments by trace element signatures. Earth Planet. Sci. Lett. 222, 43–60.

Cheng, Y.Q., Yang, C.H., Wan, Y.S., Liu, Z.X., Zhang, X.P., Du, L.L., Zhang, S.G., Wu, J.S., Gao, J.F., 2004. Precambrian Geology and Anatexis and Its Reworking in the Crustal Rocks at the Central-Northern Segments of the Taihangshan Mountain. Geol. Publ. House, Beijing 191 in Chinese.

Collerson, K.D., Kamber, B.S., 1999. Evolution of the Continents and the Atmosphere Inferred from Th-U-Nb Systematics of the Depleted Mantle. Science 283, 1519–1522.

Cui, M.L., Zhang, L.C., Wu, H.Y., Xu, Y.X., Li, W.J., 2014. Timing and tectonic setting of the Sijiaying banded iron deposit in the eastern Hebei province, North China Craton: Constraints from geochemistry and SIMS zircon U-Pb dating. J. Asian Earth Sci. 94, 240–251.
Dai, Y.P., Zhang, L.C., Wang, C.L., Liu, L., Cui, M.L., Zhu, M.T., Xiang, P., 2012. Genetic type, formation age and tectonic setting of the Waitoushan banded iron formation, Benxi. Liaoning province. Acta Petrol. Sin. 28, 3574–3594 in Chinese with English abstract.
Dai, Y.P., Zhang, L.C., Zhu, M.T., Wang, C.L., Liu, L., Xiang, P., 2014. The composition and genesis of the Mesoarchean Dagushan banded iron formation (BIF) in the Anshan area of the North China Craton. Ore Geol. Rev. 63, 353–373.
Dai, Y.P., Zhu, Y.D., Zhang, L.C., Wang, C.L., Chen, C., Xiu, D., 2016. An Overview of Studies on Preeambrian Banded Iron Formations (BIFs) in China and Abroad. Geol. Rev. 62, 735–757 in Chinese with English Abstract.
Derry, L.A., Jacobsen, S.B., 1990. The chemical evolution of Precambrian seawater: evidence from REEs in banded iron formations. Geochim. Cosmochim. Acta 54 (11), 2965–2977.
Dodd, M.S., Wang, H.Y., Li, C., Towner, M., Thomson, A.R., Slack, J.F., Wan, Y.S., Pirajno, F., Manikyamba, C., Wang, Q., Papineau, D., 2022. Abiotic anoxic iron oxidation, formation of Archean banded iron formations, and the oxidation of early Earth. Earth Planet. Sci. Lett. 584, 117469.
Dupuis, C., Beaudoin, G., 2011. Discriminant diagrams for iron oxide trace element fingerprinting of mineral deposit types. Miner. Deposita 46, 319–335.
Dymek, R.F., Klein, C., 1988. Chemistry, petrology and origin of banded iron formation lithologies from the 3800 Ma isua supracrustal belt. West Greenland. Precambrian Res. 39, 247–302.
Fitton, J.G., James, D., Leeman, W.P., 1991. Basic magmatism associated with late Cenozoic extension in the western United States: Compositional variations in space and time. J. Geophys. Res.: Solid. Earth 96, 13693–13711.
German, C.R., Elderfield, H., 1990. Application of the Ce-anomaly as a paleoredox indicator: the ground rules. Paleoceanography 5, 823–833.
German, C.R., Masuzawa, T., Greaves, M.J., Elderfield, H., Edmond, J.M., 1995. Dissolved rare earth elements in the Southern Ocean: Cerium oxidation and the influence of hydrography. Geochim. Cosmochim. Acta 59, 1551–1558.
Gross, G.A., 1980. A classification of iron formations based on depositional environments. Can. Mineral. 18, 215–222.
Groves, D.I., Santosh, M., 2021. Craton and thick lithosphere margins: the sites of giant mineral deposits and mineral provinces. Gondwana Res. 100, 195–222.
Guan, H., Sun, M., Wilde, S.A., Zhou, X.H., Zhai, M.G., 2002. SHRIMP U-Pb zircon geochronology of the Fuping Complex: implications for formation and assembly of the North China Craton. Precambrian Res. 113, 1–18.
Guo, R.R., Li, Z.H., Liu, S.W., Wang, M.J., Bao, H., Wang, W., Huang, X., Dou, Y.X., 2022. Late Neoarchean geodynamic regime of the northeastern North China Craton: Constraints from metamorphosed volcanic rocks of the Anshan-Benxi greenstone belt. Precambrian Res. 371, 106583.
Guo, J.H., O'Brien, P.J., Zhai, M.G., 2002. High-pressure granulites in the Sanggan area, North China craton: metamorphic evolution, P-T paths and geotectonic significance. J. Metamorph. Geol. 20, 741–756.
Han, C.M., Xiao, W.J., Su, B.X., Chen, Z.L., Zhang, X.H., Ao, S.J., Zhang, J.E., Zhang, Z.Y., Wan, B., Song, D.F., 2014. Neoarchean Algoma-type banded iron formations from Eastern Hebei, North China Craton: SHRIMP U-Pb age, origin and tectonic setting. Precambrian Res. 251, 212–231.
Han, C.M., Xiao, W.J., Su, B.X., Asamoah Sakyi, P., Ao, S., Zhang, J., Wan, B., Song, D.F., Zhang, Z.Y., Wang, Z.M., Ding, J.X., 2017. Neoarchean Algoma-type banded iron formation from the Northern Shanxi, the Trans-North China Orogen: SIMS U-Pb age, origin and tectonic setting. Precambrian Res. 303, 548–572.
Hou, K.J., Ma, X.D., Li, Y.H., Liu, F., Han, D., 2017. Chronology, geochemical, Si and Fe isotopic constraints on the origin of Huoqiu banded iron formation (BIF), southeastern margin of the North China Craton. Precambrian Res. 298, 351–364.
Hu, Z.C., Zhang, W., Liu, Y.S., Gao, S., Li, M., Zong, K.Q., Chen, H.H., Hu, S.H., 2015. "Wave" signal smoothing and mercury removing device for laser ablation quadrupole and multiple collector ICP-MS analysis: application to lead isotope analysis. Anal. Chem. 87, 1152–1157.
Huang, B., Kusky, T.M., Wang, L., Deng, H., Wang, J.P., Fu, D., Peng, H.T., Ning, W.B., 2019. Age and genesis of the Neoarchean Algoma-type banded iron formations from the Dengfeng greenstone belt, southern North China Craton: Geochronological, geochemical and Sm–Nd isotopic constraints. Precambrian Res. 333, 105437.
Huston, D.L., Logan, G.A., 2004. Barite, BIFs and bugs: Evidence for the evolution of the Earth's early hydrosphere. Earth Planet. Sci. Lett. 220, 41–55.
James, H.L., 1954. Sedimentary facies of iron-formation. Econ. Geol. 49, 235–293.
Jiang, C.Z., Halevy, I., Tosca, N.J., 2022. Kinetic isotope effect in siderite growth: Implications for the origin of banded iron formation siderite. Geochim. Cosmochim. Acta. 322, 260–273.
Konhauser, K.O., Planavsky, N.J., Hardisty, D.S., Robbins, L.J., Warchola, T.J., Haugaard, R., Lalonde, S.V., Partin, C.A., Oonk, P.B.H., Tsikos, H., Lyons, T.W., Bekker, A., Johnson, C.M., 2017. Iron formations: A global record of Neoarchaean to Palaeoproterozoic environmental history. Earth-Sci. Rev. 172, 140–177.
Lan, T.G., Fan, H.R., Santosh, M., Hu, F.F., Yang, K.F., Liu, Y.S., 2014a. U-Pb zircon chronology, geochemistry and isotopes of the Changyi banded iron formation in the eastern Shandong Province: constraints on BIF genesis and implications for Paleoproterozoic tectonic evolution of the North China Craton. Ore Geol. Rev. 56, 472–486.
Lan, T.G., Fan, H.R., Santosh, M., Hu, F.F., Yang, K.F., Liu, Y.S., Cai, Y.C., 2014b. Depositional environment and tectonic implications of the Paleoproterozoic BIF in Changyi area, eastern North China Craton: Evidence from geochronology and geochemistry of the metamorphic wallrocks. Ore Geol. Rev. 61, 52–72.
Lan, C.Y., Long, X.P., Zhao, T.P., Zhai, M.G., 2019a. In-site mineral geochemistry and whole-rock Fe isotopes of the quartz-magnetite-pyroxene rocks in the Wuyang area, North China Craton: Constraints on the genesis of the pyroxene-rich BIF. Precambrian Res. 333, 105445.
Lan, C.Y., Yang, A.Y., Wang, C.L., Zhao, T.P., 2019b. Geochemistry, U-Pb zircon geochronology and Sm-Nd isotopes of the Xincai banded iron formation in the southern margin of the North China Craton: Implications on Neoarchean seawater compositions and solute sources. Precambrian Res. 326, 240–257.
Li, H. M., Zhang, Z, J., Li, L. X., Zhang, Z. C., Chen, J., Yao T., 2014. Types and general characteristics of the BIF-related iron deposits in China. Ore Geol. Rev. 57, 264-287.
Li, L. X., Li. H. M., Xu. Y. X., Chen, J., Yao, T., Zhang, l. F., Yang, X. Q., Liu, J. M., 2015. Zircon growth and ages of migmatites in the Algoma-type BIF-hosted iron deposits in Qianxi Group from eastern Hebei Province, China: Timing of BIF deposition and anatexis. J. Asian Earth Sci. 113,1017-1034.
Li, L.X., Li, H.M., Liu, M.J., Yang, X.Q., Meng, X., 2016. Timing of deposition and tectonothermal events of banded iron formations in the Anshan-Benxi area, Liaoning Province, China: Evidence from SHRIMP U-Pb zircon geochronology of the wall rocks. J. Asian Earth Sci. 129, 276–293.
Li, F.B., Zhu, X.K., Ding, H.L., Zhang, K., 2022. Local hydrothermal sources for Superior-type iron formations: Insights from the Animikie Basin. Precambrian Res. 377, 106736.
Liou, P., Guo, J.H., Peng, P., Mitchell, R.N., Jiang, N., Zhai, M.G., Mao, M.X., 2022. Crustal growth of the north china craton at ca. 2.5 Ga. Sci. Bull. 67, 1553–1555.
Liu, J, W., Li, L., Li, S. R., Santosh, M., Yuan, M. W., 2022. Apatite as a fingerprint of granite fertility and gold mineralization: Evidence from the Xiaoqinling Goldfield, North China Craton. Ore Geol. Rev. 142, 104720.
Liu, Y.S., Hu, Z.C., Gao, S., Günther, D., Xu, J., Gao, C.G., Chen, H.H., 2008. In situ analysis of major and trace elements of anhydrous minerals by LA-ICP-MS without applying an internal standard. Chem. Geol. 257, 34–43.
Liu, Y.S., Hu, Z.C., Zong, K.Q., Gao, C.G., Gao, S., Xu, J., Chen, H.L., 2010. Reappraisement and refinement of zircon U-Pb isotope and trace element analyses by LA-ICP-MS. Chin. Sci. Bull. 55, 1535–1546.
Liu, L., Yang, X.Y., 2015. Temporal, environmental and tectonic significance of the Huoqiu BIF, southeastern North China Craton: Geochemical and geochronological constraints. Precambrian Res. 261, 217–233.
Liu, L., Zhang, L.C., Dai, Y.P., Wang, C.L., Li, Z.Q., 2012. Formation age, geochemical signatures and geological significance of the Sanheming BIF-type iron deposit in the Guyang greenstone belt. Inner Mongolia. Acta Petrol. Sin. 28, 3623–3637 in Chinese with English abstract.
Liu, L., Zhang, L.C., Dai, Y.P., 2014. Formation age and genesis of the banded iron formations from the Guyang Greenstone Belt, Western North China Craton. Ore Geol. Rev. 63, 388–404.
Liu, L., Zhang, H.S., Yang, X.Y., Li, Y.G., 2018. Age, origin and significance of the Wugang BIF in the Taihua complex, Southern North China Craton. Ore Geol. Rev. 95, 880–898.
K.R. Ludwig A geochronological toolkit for Microsoft Excel: Berkeley Geochronology Center Special Publication 2012 v. 4.
Ma, X.D., Fan, H.R., Santosh, M., Guo, J.H., 2014. Chronology and geochemistry of Neoarchean BIF-type iron deposits in the Yinshan Block, North China Craton: implications for oceanic ridge subduction. Ore Geol. Rev. 63, 405–417.
Manikyamba, C., Balaram, V., Naqvi, S.M., 1993. Geochemical signatures of polygenetic origin of a banded iron formation (BIF) of the Archaean Sandur greenstone belt (schist belt) Karnataka nucleus. India. Precambrian Res. 61, 137–164.
McLennan, S. M., 1989. Rare earth elements in sedimentary rocks: Influence of provenance and sedimentary processes. In: Lipin BR and McKay GA (eds.), Geochemistry and Mineralogy of Rare Earth Elements. Rev. Mineral. Geochem., 21, 169-200.
Mullen, E.D., 1983. MnO/TiO2/P2O5: a minor element discriminant for basaltic rocks of oceanic environments and its implications for petrogenesis. Earth Planet. Sci. Lett. 62, 53–62.
Pearce, J.A., 1982. Trace element characteristics of lavas from destructive plateboundaries. In: Thorpe, R.S. (Ed.), Andesites. Wiley, Chichester, pp. 525–548.
Pearce, J. A., 1996. A user's guide to basalt discrimination diagrams. In: Wyman, D.A. (Ed.), Trace Element Geochemistry of Volcanic Rocks: Applications for Massive Sulphide Exploration Geological Association of Canada, Short Course Notes, vol.12, pp. 79–113.
Pecoits, E., Gingras, M.K., Barley, M.E., Kappler, A., Posth, N.R., Konhauser, K.O., 2009. Petrography and geochemistry of the Dales Gorge banded iron formation: paragenetic sequence, source and implications for palaeo-ocean chemistry. Precambrian Res. 172, 163–187.
Peng, P., Guo, J.H., Zhai, M.G., Windly, B.F., Li, T.S., Liu, F., 2012. Genesis of the Hengling magmatic belt in the North China Craton: implications for Paleoproterozoic tectonics. Lithos 148, 27–44.
Planavsky, N., Bekker, A., Rouxel, O.J., Kamber, B., Hofmann, A., Knudsen, A., Lyons, T. W., 2010. Rare Earth Element and yttrium compositions of Archean and Paleoproterozoic Fe formations revisited: New perspectives on the significance and mechanisms of deposition. Geochim. Cosmochim. Acta 74, 6387–6405.
Ren, L.D., Geng, Y.S., Du, L.L., Wang, Y.B., Guo, J.J., 2013. SHRIMP data on zircons from the Wanzi series: Constraints on the rock formation time and implications of migmatization at 2.1-2.0 Ga in the Fuping Complex, North China Craton. J. Asian Earth Sci. 72, 203–215.
Rudnick, R.L., Fountain, D.M., 1995. Nature and composition of the continental crust: a lower crustal perspective. Rev. Geophys. 33, 267–309.
Santosh, M., Groves, D.I., 2022. Global metallogeny in relation to secular evolution of the Earth and supercontinent cycles. Gondwana Res. 107, 395–422.

Santosh, M., Yang, Q.Y., Teng, X., Tang, L., 2015. Paleoproterozoic crustal growth inthe North China Craton: evidence from the Lüliang Complex. Precambrian Res. 263, 197–231.
Santosh, M., Teng, X.M., He, X.F., Tang, L., Yang, Q.Y., 2016. Discovery of Neoarchean suprasubduction zone ophiolite suite from Yishui complex in the North China Craton. Gondwana Res. 38, 1–27.
Shi, Z.Q., Shi, R.Y., 2016. SHRIMP U-Pb Ages of Zircons from Banded Magnetite Quartzite of Shachang Formation in Miyun Area of Beijing and Their Significance. J. Earth Sci. Environ. 38, 547–557 in Chinese with English abstract.
Shi, Z.Q., Shi, R.Y., 2017. Formation and Metamorphic Ages of the Banded Iron Formation in Fangmayu of Miyun, Beijing: Zircon SHRIMP U-Pb Dating. Geoscience 31, 1–10 in Chinese with English abstract.
Shi, K.X., Wang, C.M., Bagas, L., Du, B., Yang, L.F., Chen, Q., 2019. Genesis of the Hanwang Fe deposit in Neoarchean granite-greenstone succession of the eastern North China Craton. Ore Geol. Rev. 105, 387–403.
Sindhuja, C.S., Manikyamba, C., Pahari, A., Satyanarayanan, M., 2020. Geochemistry of banded sulphidic cherts of Sandur greenstone belt, Dharwar Craton, India: Constraints on hydrothermal processes and gold mineralization. Ore Geol. Rev. 122, 103529.
Sugitani, K., 1992. Geochemical characteristics of Archean cherts and other sedimentary rocks in the Pilbara Block, Western Australia: evidence for Archean seawater enriched in hydrothermally-derived iron and silica. Precambrian Res. 57, 21–47.
Sun, S.S., McDonough, W.F., 1989. Chemical and isotopic systematics of oceanic basalts: implications for mantle composition and processes. Geol. Soc. Lond. Spec. Publ. 42, 313–345.
Sun, X.H., Tang, H.S., Luan, Y., Chen, J.H., 2020. Geochronological constraints on the genesis of high-grade iron ore in the Gongchangling BIFs from the Anshan-Benxi area. North China Craton. Ore Geol. Rev. 122, 103504.
Sun, H.T., Wu, J.R., Yu, P.S., Li, J.P., 1998. Geology, geochemistry and sulfur isotope composition of the Late Proterozoic Jingtieshan (Superior-type) hematite–jasper–barite iron ore deposits associated with strata-bound Cu mineralization in the Gansu Province. China. Miner. Deposita 34, 102–112.
Tang, L., Santosh, M., 2018a. Neoarchean-Paleoproterozoic terrane assembly and Wilson cycle in the North China Craton: an overview from the central segment of the TransNorth China Orogen. Earth-Sci. Rev. 182, 1–27.
Tang, L., Santosh, M., 2018b. Neoarchean granite-greenstone belts and related ore mineralization in the North China Craton: An overview. Geosci. Front. 9, 751–768.
Tang, L., Santosh, M., Teng, X.M., 2015. Paleoproterozoic (ca. 2.1-2.0 Ga) arc magmatism in the Fuping complex: implications for the tectonic evolution of the Trans-north China Orogen. Precambrian Res. 268, 16–32.
Tang, L., Santosh, M., Tsunogae, T., Teng, X.M., 2016. Late Neoarchean arc magmatism and crustal growth associated with microblock amalgamation in the north China Craton: evidence from the Fuping complex. Lithos. 248–251, 324–338.
Tang, L., Santosh, M., Tsunogae, T., Koizumi, T., Hu, X.K., Teng, X.M., 2017. Petrology, phase equilibria modelling and zircon U-Pb geochronology of Paleoproterozoic mafic granulites from the Fuping complex, north China Craton. J. Metamorph. Geol. 35, 517–540.
Tang, L., Santosh, M., Palin, R.M., Jia, L.H., Cao, H.W., Sheng, Y.M., 2023. Long-lived (>100 m.y.) postcollisional exhumation and cooling in the Paleoproterozoic Trans-North China orogen: Evidence from phase equilibria modeling and monazite petrochronology of granulite-facies metapelites in the Fuping Complex. Geol. Soc. Am. Bull. https://doi.org/10.1130/B36623.1.
Tong, X.X., Wang, C.L., Peng, Z.D., Huang, H., Zhang, L.C., Zhai, M.G., 2019. Geochemistry of meta-sedimentary rocks associated with the Neoarchean Dagushan BIF in the Anshan-Benxi area, North China Craton: Implications for their provenance and tectonic setting. Precambrian Res. 325, 172–191.
Trap, P., Faure, M., Lin, W., Monie, P., 2007. Late Paleoproterozoic (1900–1800 Ma) nappe stacking and polyphase deformation in the Hengshan-Wutaishan area: implications for the understanding of the Trans-North-China Belt. North China Craton. Precambrian Res. 156, 85–106.
Trap, P., Faure, M., Lin, W., Le Breton, N., Monié, P., 2012. Paleoproterozoic tectonic evolution of the Trans-north China Orogen: toward a comprehensive model. Precambrian Res. 222, 191–211.
Veizer, J., 1983. Geologic evolution of the Archean-Early Proterozoic Earth. In: Schopf, J. W. (Ed.), Earth's Earliest Biosphere. Princeton, Princeton University Press, pp. 240–259.
Wang, C, L., Zhang, L. C., Dai, Y. P., Lan, C. Y., 2015. Geochronological and geochemical constraints on the origin of clastic meta-sedimentary rocks associated with the Yuanjiacun BIF from the Lüliang Complex, North China. Lithos 212, 231-246.
Wang, J.Y., Li, Z.D., Li, G.Y., Wen, S.B., Xie, Y., Zhang, Q., Zhang, F., Ding, N., 2020b. Formation Age, Geochemical Signatures and Geological Significance of the Hejiao Iron Deposit. Inner Mongolia. Earth Sci. 45, 2135–2151 in Chinese with English abstract.
Wang, J.L., Yang, C.H., Wyman, D.A., Song, H.X., Du, L.L., 2020a. Petrogenesis and tectonic implications of the 2.1–2.0 Ga granitoids in Fuping Complex, North China Craton: Constraints from petrology, geochemistry and zircon U-Pb-Hf isotopes. Precambrian Res. 339, 105611.
Wang, C.L., Zhang, L.C., Lan, C.Y., Dai, Y.P., 2014. Petrology and geochemistry of the Wangjiazhuang banded iron formation and associated supracrustal rocks from the Wutai greenstone belt in the North China Craton: Implications for their origin and tectonic setting. Precambrian Res. 255, 603–626.
Wei, C., Qian, J., Zhou, X., 2014. Paleoproterozoic crustal evolution of the Hengshan–Wutai–Fuping region, north China Craton. Geosci. Front. 5, 485–497.
Wonder, J., Spry, P., Windom, K., 1988. Geochemistry and origin of manganese-rich rocks related to iro-formation and sulfide deposits, western Georgia. Econ. Geol. 83, 1070–1081.
Wu, J.S., Geng, Y.S., Shen, Q.H., Wan, Y.S., Liu, D.Y., Song, B., 1998. Archaean geology characteristics and tectonic evolution of China-Korea Paleo-continent. Geol. Publ. House, Beijing 192–211 in Chinese.
Xia, X., Sun, M., Zhao, G.C., Wu, F.Y., Xu, P., Zhang, J., He, Y., Zhang, J., 2006. U-Pb Age and Hf Isotope Study of Detrital Zircons from the Wanzi Supracrustals: Constraints on the Tectonic Setting and Evolution of the Fuping Complex, Trans-North China Orogen. Acta Geol. Sin. 80, 844–863. English Edition.
Y.X. Xu Y. Zhang B. Yang X.W. Bao Phanerozoic Evolution of Lithospheric Structures of the North China Craton Geophys. Res. Lett. 49 2022 e2022GL098341.C.
Yang, X.Y., Liu, L., Lee, I., Wang, B.H., Du, Z.B., Wang, Q.C., Wang, Y.X., Sun, W.D., 2014. A review on the Huoqiu banded iron formation (BIF), southeast margin of the North China Craton: Genesis of iron deposits and implications for exploration. Ore Geol. Rev. 63, 418–443.
Zhai, M.G., Santosh, M., 2013. Metallogeny of the North China Craton: Link with secular changes in the evolving Earth. Gondwana Res. 24, 275–297.
Zhai, M.G., Bian, A.G., Zhao, T.P., 2000. The amalgamation of the supercontinent of North China Craton at the end of neo-archaean and its breakup during late palaeoproterozoic and mesoproterozoic. Sci. China. Ser. D: Earth Sci. 43, 219–232 in Chinese with English Abstract.
Zhai, M.G., Santosh, M., 2011. The Early Precambrian odyssey of the North China Craton: a synoptic overview. Gondwana Res. 20, 6–25.
Zhai, M.G., Zhao, L., Zhu, X.Y., Zhou, Y.Y., Peng, P., Guo, J.H., Li, Q.L., Zhao, T.P., Lu, J. S., Li, X.H., 2021. Late Neoarchean magmatic – metamorphic event and crustal stabilization in the North China Craton. Am. J. Sci. 321, 206–234.
Zhang, F.Q., Liu, J.Z., Ouyang, Z.Y., 1998. Tectonic framework of greenstones in the basement of the North China Craton. Acta Geophys. Sin. 41, 99–107 in Chinese with English Abstract.
Zhang, L.C., Zhai, M.G., Zhang, X.J., Xiang, P., Dai, Y.P., Wang, C.L., Pirajno, F., 2012b. Formation age and tectonic setting of the Shirengou Neoarchean banded iron deposit in eastern Hebei Province: Constraints from geochemistry and SIMS zircon U-Pb dating. Precambrian Res. 222–223, 325–338.
Zhang, X.J., Zhang, L.C., Xiang, P., Wan, B., Pirajno, F., 2011. Zircon U-Pb age, Hf isotopes and geochemistry of Shuichang Algoma-type banded iron-formation, North China Craton: constraints on the ore-forming age and tectonic setting. Gondwana Res. 20, 137–148.
Zhang, J., Zhao, G.C., Li, S.Z., Sun, M., Chan, L.S., Shen, W.L., Liu, S.W., 2012a. Structural pattern of the Wutai complex and its constraints on the tectonic framework of the Trans-North China Orogen. Precambrian Res. 222–223, 212–229.
Zhao, G.C., Wilde, S.A., Cawood, P.A., Lu, L.Z., 2000. Petrology and P-T path of the Fuping mafic granulites: implications for tectonic evolution of the central zone of the North China Craton. J. Metamorph. Geol. 18, 375–391.
Zhao, G.C., Sun, M., Wilde, S.A., Li, S., 2005. Late Archean to Paleoproterozoic evolution of the North China Craton: key issues revisited. Precambrian Res. 136, 177–202.
Zhao, G.C., Cawood, P.A., Li, S.Z., Wilde, S.A., Sun, M., Zhang, J., He, Y.H., Yin, C.Q., 2012. Amalgamation of the North China Craton: key issues and discussion. Precambrian Res. 222–223, 55–76.
Zhao, G.C., Zhai, M.G., 2013. Litho tectonic elements of Precambrian basement in the North China Craton: review and tectonic implications. Gondwana Res. 23, 1207–1240.
Zhao, G.C., Wilde, S.A., Cawood, P.A., Sun, M., 2002. SHRIMP U-Pb zircon ages of the Fuping Complex: implications for Late Archean to Paleoproterozoic accretion and assembly of the North China Craton. Am. J. Sci. 302, 191–226.
Zhao, G.C., Kroener, A., Wilde, S.A., Sun, M., Li, S., Li, X., Zhang, J., Xia, X., He, Y., 2007. Lithotectonic elements and geological events in the hengshan–wutai–fuping belt: a synthesis and implications for the evolution of the Trans-North China Orogen. Geol. Mag. 144, 753–775.
Zhu, M.T., Dai, Y.P., Zhang, L.C., Wang, C.L., Liu, L., 2015. Geochronology and geochemistry of the Nanfen iron deposit in the Anshan-Benxi area, North China Craton: Implications for ~2.55 Ga crustal growth and the genesis of high-grade iron ores. Precambrian Res. 260, 23–38.
Zong, K.Q., Klemd, R., Yuan, Y., He, Z.Y., Guo, J.L., Shi, X.L., Liu, Y.S., Hu, Z.C., Zhang, Z.M., 2017. The assembly of Rodinia: The correlation of early Neoproterozoic (ca. 900 Ma) high-grade metamorphism and continental arc formation in the southern Beishan Orogen, southern Central Asian Orogenic Belt (CAOB). Precambrian Res. 290, 32–48.